國 立 交 通 大 學

光 電 工 程 研 究 所

碩 士 論 文

利用同調兆赫光譜技術研究Ⅲ族氮化物的光電特性

Coherent THz Spectroscopic Studies of Group III-Nitride Compound Semiconductors

研 究 生：顧昀浦

指導教授：潘犀靈 教授

安惠榮 教授

中 華 民 國 九 十 六 年 七 月

利用同調兆赫光譜技術研究Ⅲ族氮化物的光電特性

Coherent THz Spectroscopic Studies of Group III-Nitride Compound Semiconductors

研 究 生：顧昀浦　　Student：Yun-Pu Ku

指導教授：潘犀靈 教授　　Advisors：Prof. Ci-Ling Pan

安惠榮 教授　　Prof. Hyeyoung Ahn

國立交通大學

光電工程研究所

碩士論文

A Thesis
Submitted to Department of Photonics and
Institute of Electro-Optical Engineering
College of Electrical Engineering
National Chiao Tung University
In partial Fulfillment of the Requirements
for the Degree of
Master of Science
in

Electro-Optical Engineering

July 2007
Hsinchu, Taiwan, Republic of China

中 華 民 國 九 十 六 年 七 月

利用同調兆赫光譜技術研究Ⅲ族氮化物的光電特性

學生：顧昀浦　　指導教授：潘犀靈教授
安惠榮教授
國立交通大學光電工程研究所

摘　要

我們利用同調兆赫光譜技術研究氮化鎵與氮化銦薄膜和奈米柱樣品在兆赫波段的響應，進而求得樣品的折射係數和導電率，並成功的使用簡單 Drude 模型來擬合氮化鎵與氮化銦薄膜的導電率得到良好的結果，但氮化銦奈米柱量測結果與簡單 Drude 模型的預測有偏差，而使用經修正的 Drude-Smith 模型可得到良好的擬合結果，根據擬合所得的參數可以計算出樣品的載子的飄移率和濃度且跟霍爾量測所得的結果相符。

利用時間解析的光激發兆赫波探測技術，我們也研究氮化銦薄膜和其奈米柱的瞬時載子特性，並發現在奈米柱中的載子有較短的生命期，推測是因奈米柱的結構會產生較多的缺陷而使得載子有較快的捕捉時間，而奈米柱結構在光激發後會有較低的光導電率則是因為光電子會因為量子侷限效應而有較低的漂移率所致。

我們並利用氮化銦薄膜和奈米柱作為兆赫波的光激發射器，研究其兆赫輻射特性。與薄膜相比，實驗結果顯示奈米柱的結構輻射強度提高達三倍以上，並跟奈米柱的直徑大小有關。因為表面空乏區的電場會遮蔽住產生主要輻射的 Photo-Dember 電場，所以當奈米柱直徑遠大於表面空乏區深度時，可以更有效率的發射出兆赫波。

Coherent THz Spectroscopic Studies of Optoelectronic Properties of Group III-Nitride Compound Semiconductors

Student：Yun-Pu Ku

Advisors：Prof. Ci-Ling Pan
Prof. Hyeyoung Ahn

Department of Photonics and Institute of Electro-Optic Engineering, College of Electrical Engineering
National Chiao Tung University

Abstract

Terahertz time-domain spectroscopy (THz-TDS) has been used to investigate THz conductivity of group III-nitride compound semiconductors and their nanostructures including gallium nitride (GaN) and indium nitride (InN). THz conductivities of GaN and InN films are well fitted by the simple-Drude model, while negative imaginary conductivity of InN nanorods should be fitted using the Drude-Smith model. The carrier mobility and concentration of each sample are obtained from the fit parameters.

Transient carrier dynamics of InN film and nanorods have been investigated by optical pump-terahertz probe technique. The faster carrier trapping time of nanorods is attributed to the morphology of nanorods with a considerable amount of the defect and trap states. The reduced photoconductivity of nanorods is due to the confinement of excited carriers inside the nanorods.

We have also studied terahertz emission from InN nanorods and InN film. THz emission from InN nanorods is at least three times more intense than that from InN film and depends strongly on the size distribution of the nanorods. Surface electron accumulation at the InN nanorods effectively screens out the photo-Dember field in the accumulation layer formed under the surface. The nanorods with considerably large diameter than the thickness of accumulation layer contribute dominantly in the emission of THz radiation from InN nanorods arrays.

Acknowledgement

在兩年的研究生活中，過程雖然艱辛，但也使我獲得了很大的成長，並讓我體會到了研究的迷人和辛苦之處。這本論文能夠完成首先要感謝我的指導老師潘犀靈教授和安惠榮教授無私的指導，給予我研究的方向和教導我研究該有的態度和觀念。還要感謝交大郭浩中老師和清大果尚志老師實驗室提供我實驗所需的樣品和在量測與製程上的幫助。還要感謝王怡超學長，在系統的架設與實驗室事務上的指導與幫忙，謝卓帆學長在系統使用上的教導，此外還要感謝和我一起奮鬥的五位同學，君豪，彥毓，哲睿，韋文，宜貞，除了提供我學業上的討論外也增添了不少生活上的樂趣。最後要感謝的是一路支持我的家人，沒有你們就沒有這本論文。

Contents

List of Figures

List of Tables

1. Introduction

1.1 Terahertz Radiation

Terahertz (THz) radiation lies in the frequency gap between the infrared and microwaves(see Fig. 1.1), typically is referred to as the frequencies from 100 GHz to 30 THz. 1 THz is equivalent to 33.33 cm^{-1}(wave numbers), 4.1 meV photon energy, or 300 μm wavelength. Before 1980s people don't know much about THz because the generation and detection technologies are not well established, but since the development of femtosecond laser, THz has been intensely studies. At middle 1980s, Auston [1] successfully used photoconductive dipole antenna to generate and detect coherently THz radiation in time domain, and this technology is called THz time-domain spectroscopy (THz-TDS). After Auston's research many other generation methods have been developed including optical rectification [2], surge current in semiconductor surface [3], quantum cascade laser [4]…, and in 1995 XC-Zhang *et al*[5] successfully used ZnTe crystal to detect THz radiation by free-space electro-optic sampling that highly increased the detection bandwidth and signal to noise ratio.

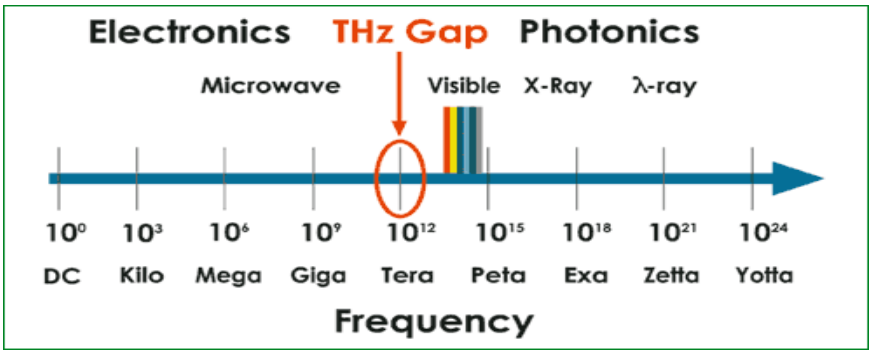

Fig.1-1 The spectrum range of electromagnetic waves
(http://www.rpi.edu/terahertz/about_us.html)

Terahertz has much smaller photon energy (4.1 meV) compared to X-ray and therefore this kind of non-destruction measurement can be used for biology and

medical sciences [6]. Image and tomography [7] of THz have also been studied and can be applied to homeland security.

For semiconductors measurement, conventional four point probe and Hall effect measurement can measure the characteristics including mobility, carrier concentration and resistivity of the semiconductor materials by direct sample contact. All these electrical measurements measure only DC value of the sample but some characteristics (refractive index, conductivity) are frequency-dependent. For some semiconductors with high resistivity and low concentration, the electrical properties are difficult to be measured by simple direct contact because at the metal-semiconductors interface, the Schottky barrier may disturb the measurement value. Therefore, THz-TDS with advantages of non-contact and frequency-dependant measure is desirable for semiconductors characterization. In 1990 D. Grischkowsky *et al* [8] successfully measured optical properties including refractive index and conductivity of GaAs wafer and the results fit well with the Drude model. Besides GaAs, other semiconductors such as silicon [9] have also been widely studied. Recently, many nanostructured semiconductors like InP-nanoparticle [10], ZnO-nanowire [11], Si-nanoparticle [12] have been studied using THz-TDS technology and the particular conduction behavior have been observed. In comparison with conventional far-IR source and detector, THz-TDS is a coherent technology that means both amplitude and phase information can be obtained. Both absorption coefficient and refractive index could be extracted without use of Kramers-Kronig relation that simplifies the analysis process.

1.2 III-Nitride Compound Semiconductors

Group-III nitride semiconductors and their alloys have attracted a lot of attention due to their unique properties for fundamental research and potential applications. Recent research has shown that the bandgap of InN is actually 0.7 eV [13]. Alloyed with GaN, the ternary system InGaN has been shown to cover a wide, continuous spectral range from the near infrared for InN to the near ultraviolet for GaN. Currently there is research into developing solar cells using the nitride based semiconductors. Using the alloy indium gallium nitride, an optical match to the solar spectrum is obtained (see Fig. 1-2). Thus, in this work, we focus on the properties of GaN and InN.

1.2.1 GaN

Gallium nitride is a direct bandgap semiconductor material of wurtzite crystal structure with a wide (3.4 eV) band gap. It has been intensely studied over the last ten years. GaN has multiple applications in blue LEDs and laser diodes and also attracts much attention as one of the promising materials for high-power transistors operating at the wavelengths in the millimeter and sub-millimeter regions because of its large breakdown voltage. Besides, another potential application of GaN is as an alternative substrate for THz photoconductive antenna. Because it has much bigger breakdown voltage and electron saturation velocity in comparison with conventional GaAs substrate and therefore the electrode bias can be increased by about a factor of eight. The output power of THz radiation is proportional to the square of the bias and thus higher power THz radiation may be achievable.

1.2.2 InN

Indium nitride (InN) is an interesting and potentially important semiconductor material with superior electronic transport properties over other group-III nitrides.

Recently, low-dimensional InN nanomaterials in the forms of nanowires, nanorods, nanotubes, etc. have received great attention due to their potential in near-infrared (NIR) optoelectronics. And they are also good candidates for photovoltaic materials. The discovery of the intrinsic narrow bandgap (0.7 eV) and remarkably large gap (2.8 eV) between the conduction band minimum and the next local minimum of InN also inspires potential applications in the terahertz (THz) range, for example as an efficient THz emitter/detector. There have been several reports on THz emission from InN films [14] [15] [16]. The THz radiation emitted from InN films is typically one order of magnitude weaker than that from InAs, although the main THz emission mechanism of both materials is the photo-Dember effect. In particular, Pradarutti *et al*. [16] showed that THz emission from InN depends on the growth method and the surface morphology of samples. In their study, THz emission from an InN film with strong columnar morphology was found to be about one order of magnitude smaller than that from the InN film with smooth surface. Due to the increased effective emitting surface area, however, nanostructured InN is expected to emit stronger THz signal than the epilayer.

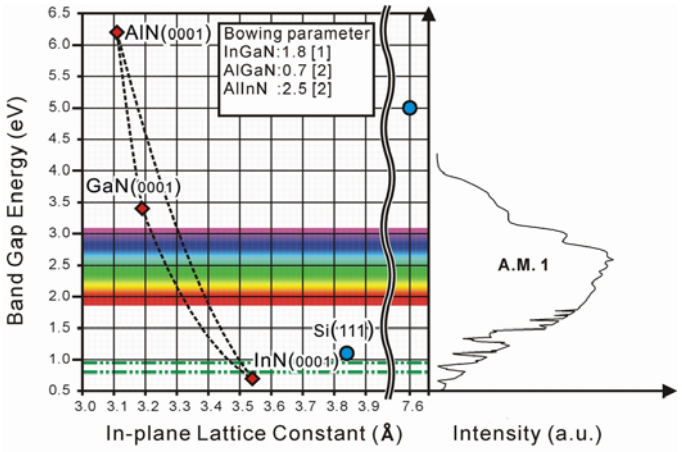

Fig.1-2 The energy band gaps of Group-III nitride semiconductors. The ternary system InGaN can match the solar spectral irradiance as shown at the right side.

1.3 Organization of this Thesis

In chapter 1, an overview of THz radiation and Ⅲ-Nitride compound semiconductors are presented. In chapter 2, the experimental theories including THz radiation and detection, and analysis methods are interpreted. In chapter 3, the basic characteristics including growth method and Hall measurement results of the semiconductor samples studied in this thesis are described. In chapter 4, the experimental setups including the laser system and two THz-TDS systems are introduced. The experimental results and discussion will be presented in chapter 5. Finally, our conclusions and future work are shown in chapter 6.

2. Experimental Theories

2.1 Terahertz Generation

Many methods have been exploited to develop sources of pulsed THz for the past two decades because of the development of ultrafast laser. The most common mechanism are surge current and transient polarization which acts as broadband terahertz sources. The radiation is then directly emitted into free space or coupled out with an antenna. In this work, the THz waves are generated via surge current, therefore we focus on this mechanism in this section. Basic mechanism of surge current begins with an ultrashort laser pulse which creates electron-hole pairs in semiconductors. Then the carriers accelerate in the external or internal electrical field to form a transient current which radiate THz waves. In the far field approximation, the field amplitude of the radiation is proportional to the time derivative of the photo-current.

2.1.1 Surge-Current Model

From Maxwell's equation, we have two inhomogeneous wave equations in terms of magnetic potential $\vec{A}$ and electric potential V [17]:

$$\nabla^2 \vec{A} - \varepsilon\mu \frac{\partial^2 \vec{A}}{\partial t^2} = -\mu \vec{J} \tag{2.1}$$

$$\nabla^2 V - \varepsilon\mu \frac{\partial^2 V}{\partial t^2} = -\frac{\rho}{\varepsilon} \tag{2.2}$$

where $\vec{J}$ is the current density and ρ is the charge density. These equations describe the propagation of the electromagnetic disturbances. In terms of these potential, the electric field $\vec{E}$ is expressed as

$$\vec{E} = -\nabla V - \frac{\partial \vec{A}}{\partial t} \tag{2.3}$$

The continuity equation of free carriers which is generated in the emitter after the absorption of an optical pulse is obtained directly from Maxwell's equation:

$$\nabla \cdot (\nabla \times \vec{H}) = \nabla \cdot (J + \frac{\partial \vec{D}}{\partial t}) = \nabla \cdot \vec{J} + \frac{\partial \rho}{\partial t} = 0 \qquad (2.4)$$

The current is a transverse current which is perpendicular to the direction of propagation, so that we have $\nabla \cdot \vec{J}$=0. Eq (2.1) and Eq (2.4) imply that the charge density is constant in time and will not contribute to the time dependent radiated electric field. Therefore, from Eq (2.3) we have

$$E_{rad}(t) = -\frac{\partial}{\partial t}\vec{A}(t) \qquad (2.5)$$

The solution to the wave equation (2.1) and hence for the vector potential $\vec{A}$ leads to the expression for the time-dependent radiated electric field $E_{rad}(\vec{r},t)$ at a displacement $\vec{r}$ from the center of the emitter:

$$\vec{E}_{rad}(\vec{r},t) = -\frac{1}{4\pi\varepsilon_0 c^2}\frac{\partial}{\partial t}\int \frac{J_s(\vec{r}', t - \frac{|\vec{r}-\vec{r}'|}{c})}{|\vec{r}-\vec{r}'|} da' \qquad (2.6)$$

where ε_0 is the permittivity of free space, c is speed of light in vacuum, $\vec{J}_s$ is the surface current in emitter evaluated at the retarded time, and da' is the increment of surface area at a displacement $\vec{r}'$ from the center of the emitter. In the far field and assuming $\vec{J}_s$ is a constant at all points in the emitter, the radiated field can be written as

$$\vec{E}_{rad}(\vec{r},t) = \frac{b}{r}\frac{d}{dt}\vec{J}_s(t) \qquad (2.7)$$

where b is a constant, and the radiated field is proportional to the time derivative of photo-current.

2.1.2 Photoconductivity Antenna

After the pioneering research by Auston *et al* [1], the technique for generating pulsed terahertz radiation using femtosecond laser pulses has been studied intensively. Photoconductive antenna is one of the most commonly used emitter and detector as well as Electro-Optic crystals. There are two important features of photoconductive antenna: a suitable substrate and an antenna structure. The antenna is illuminated by an ultrashort laser pulse with photon energy higher than substrate bandgap, and the electron-hole pairs are created. The free carriers then accelerate in the static bias field to form a transient photo-current, and the fast, time-varying current radiates THz waves as shown in Fig. 2-1.

THz radiation is affected by several substrate parameters and antenna structure. For high efficiency THz radiation, the substrates such as InP with small effective electron mass which can provide rapid photocurrent rise and decay times are desirable. The mobility also plays an important role and is limited by carrier intraband and intervalley scattering. However, to generate strong THz emission, it is necessary to apply the voltage bias as high as possible without saturation. Thus, the resistivity of substrate usually is most important for emission efficiency. In this sense, LT-GaAs with extraordinary high resistivity and reasonable good mobility is widely used. Antenna structure design influence the bandwidth and waveform of THz radiation, and three of the most commonly used design are dipole, stripline, and bow-tie type antennas.

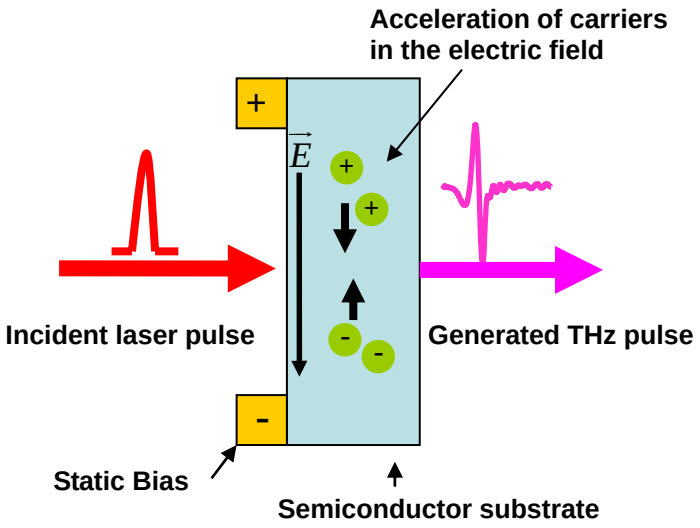

Fig.2-1 Schematic figure of THz generation from photoconductive antenna

2.1.3 Surface Depletion Field

In semiconductors with wide bandgaps such as GaAs (1.43 eV) and InP (1.34 eV), there may exist surface states in the forbidden gaps between valance and conduction bands because of the discontinuous structures in the surface. These states may be occupied or vacant, and therefore affect the equilibrium concentration of electrons and holes in the surface. Because the Fermi-level is position independent, the energy bands must bend to form a depletion region where the surface built-in field exists as shown in Fig. 2-2. The field direction is normal to the surface, and strength is a function of Schottky [18] barrier potential and dopant concentration Eq (2.8).

$$E_d(x) = \frac{eN}{\varepsilon}(W - x) \qquad (2.8)$$

Where N is dopant concentration, ε is semiconductor permittivity, and W is depletion width and has the form of Eq (2.9)

$$W = \sqrt{\frac{2\varepsilon}{eN}[V - \frac{kT}{e}]} \qquad (2.9)$$

Where V is the potential barrier and kT/e is the thermal energy. In general, the

energy band is bent upward and downward for n-type and p-type semiconductors, respectively. After photon excitation, the electrons and holes are accelerated in opposite direction by the built-in field to drive a surge current. The decay time of photo-current is equal to the carrier life time or the transmit time of free carriers crossing the depletion width. Thus the transient current radiates THz waves.

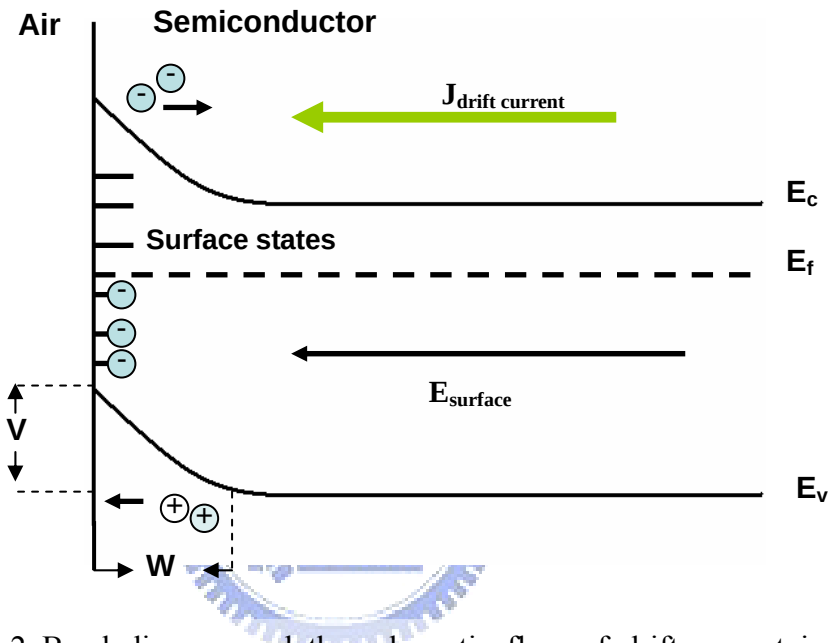

Fig.2-2 Band diagram and the schematic flow of drift current in a typical n-type semiconductor.

2.1.4 Photo-Dember Effect

Some semiconductors such as InAs and InSb with small band gap and effective electron mass radiate THz via Photo-Dember effect. The band bending in this kind of semiconductors is not obvious resulting in a relative small surface depletion field. The high absorption coefficient due to a small bandgap causes a large gradient carrier concentration after excitation by ultrafast laser pulse. The excited electrons and holes diffuse in the same direction but with different velocities, and therefore the Photo-Dember effect dominant (Fig.2-3). Because the electron mobility is always large than hole mobility, the photo-current is always in the same direction

for both n- or p-type semiconductors. The fast photo-current rise and decay time due to the small electron mass and high mobility which often increase with decreasing band gap is helpful for efficient THz generation. Another advantage of this mechanism is the need of photon energy is comparable small that make the free carriers have large excess energy. The photo-Dember voltage can be expressed by [19]:

$$V_D = \frac{k_B(T_e b - T_h)}{e}\frac{1}{b+1}\ln(1+\frac{(b+1)\Delta n}{n_0 b + p_0}) \qquad (2\text{-}10)$$

Where n_0 and p_0 are the intrinsic concentration of the electrons and holes, b is the mobility ratio $b = \mu_e / \mu_p$, and T_e and T_h are the temperature of photo-excited electrons and holes, respectively. From Eq (2-10) several properties can be deduced: high electron temperature, mobility ratio b and low intrinsic carrier concentration can enhance the Photo-Dember voltage. The corresponding electric field ($E_D = V_D/d$, d is absorption length) is enhanced by decreasing absorption length. Thus, the Photo-Dember effect is much stronger in narrow bandgap materials (InAs) than in wide badgap materials (GaAs). Recently, InAs has been reported as a strong THz emitter with intensity at least one order of magnitude higher than other unbiased semiconductor emitters such as InP and GaAs. Therefore, high conversion efficiency has made InAs received much attention and be one of the most widely used THz emitters.

InN has also been considered to generate THz waves via Photo-Dember effect [15], and we will discuss it in chapter 5.

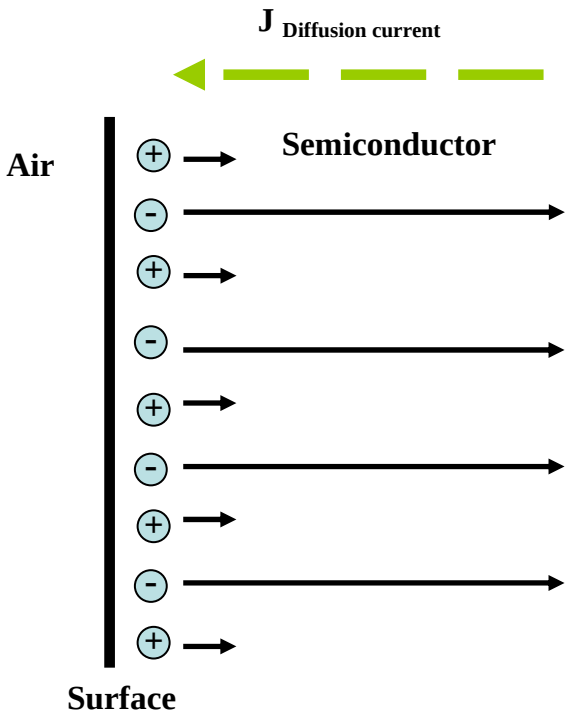

Fig.2-3 Schematic flow of diffusion current by photo-excited carriers near the surface of a semiconductor

2.2 Terahertz Detection

The most common methods for THz detection are photoconductive sampling and electro-optic sampling. Both of them are coherent detection which indicate both amplitude and phase information can be obtained at the same by scanning the THz time-domain waveform and have high signal to noise ratio in comparison with bolometer. Their properties are described below.

2-2-1 Photoconductive Sampling

The mechanism of photoconductive detection is inverse to that of photoconductive emission. The unbiased antenna is illuminated collinearly by the THz pulse and an ultrafast laser pulse, and the generated photo-carriers are accelerated by the THz electric field to form a current. Because the laser pulse has much shorter duration than the THz pulse and the photo-current is proportional to the THz electrical field because of Ohm's law, we can measure the photo-current as a function of delay time between the THz pulse and the probe laser pulse, and therefore the entire THz time-domain waveform can be obtained. Photoconductive sampling has high SNR in low-frequency THz signal, but the performance dramatically decreases for frequency above several THz because the resonant behavior of the Hertzian dipole structure limits the detection bandwidth. Photoconductive sampling is usually used for oscillator, non-amplified, laser system because of the need of focus on the antenna.

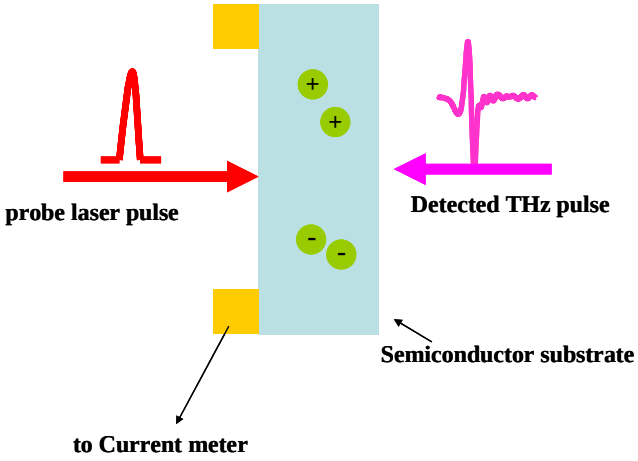

Fig. 2-4 Schematic figure of photoconductive detection.

2.2.2 Electro-Optic Sampling

When using an amplified laser system, the THz pulses are best detected via free space electro-optic sampling rather than photoconductive antennas, because the need of focused beam is not necessary that decrease the potential for damaging the material. It is a nonresonant method and is suitable for broadband detection [20]. The THz beam is focused onto an EO crystal and modify the index ellipsoid transiently, via Pockels effect. The linearly polarized laser probe beam copropagate inside the crystal with the THz beam, and its phase is modulated by the refractive index change induced by the electric field of the THz pulse as shown in Fig. 2-5.

The principle can be explained as follow. Suppose z is the probe beam propagating direction, and x and y are the crystal axes of the EO crystal (see Fig. 2-5). When an electric field is applied to the EO crystal, the birefringence axes induced by electric field x' and y' are at an angle of 45° with respect to x and y axes. If the input probe beam is polarized along x with E_0 amplitude, then the output beam can be expressed by

$$\begin{pmatrix} E_x \\ E_y \end{pmatrix} = \begin{pmatrix} \cos\frac{\pi}{4} & -\sin\frac{\pi}{4} \\ \sin\frac{\pi}{4} & \cos\frac{\pi}{4} \end{pmatrix} \begin{pmatrix} \exp(i\delta) & 0 \\ 0 & 1 \end{pmatrix} \begin{pmatrix} \cos\frac{\pi}{4} & \sin\frac{\pi}{4} \\ -\sin\frac{\pi}{4} & \cos\frac{\pi}{4} \end{pmatrix} \begin{pmatrix} E_0 \\ 0 \end{pmatrix} = \frac{E_0}{2} \begin{pmatrix} \exp^{i\delta}+1 \\ \exp^{i\delta}-1 \end{pmatrix} \quad (2\text{-}11)$$

Where $\delta = \Gamma_0 + \Gamma$ is the phase difference between the x' and y' polarizations, including both the dynamic term, Γ, induced by THz field and the static term, Γ_0. The intensity of probe beam in x and y direction can be expressed by

$$I_x = |E_x|^2 = I_0 \cos^2 \frac{\Gamma + \Gamma_0}{2}$$
$$I_y = |E_y|^2 = I_0 \sin^2 \frac{\Gamma + \Gamma_0}{2} \quad (2\text{-}12)$$

Where $I_0=E_0^2$ is the input intensity and $I_x+I_y=I_0$ is the result of energy conservation. To extract the I_x and I_y independently, a Wollaston prism is usually used. The static phase difference term Γ_0 is often set at $\pi/2$ by a quarter-wave plate for balance detection. In most cases of EO sampling, Γ is much smaller than 1($\Gamma << 1$), so we have

$$I_x = \frac{I_0}{2}(1-\Gamma)$$
$$I_y = \frac{I_0}{2}(1+\Gamma) \quad (2\text{-}13)$$

We can measure the signal difference, I_s, between I_x and I_y by a balance detector, and therefore we have:

$$I_s = I_y - I_x = I_0\Gamma \quad (2\text{-}14)$$

The signal difference is proportional to the phase change Γ induced by THz field, for a (110) oriented ZnTe crystal, the phase change term Γ can be expressed by

$$\Gamma = \frac{\pi d n^3 \gamma_{41}}{\lambda} E \quad (2\text{-}15)$$

Where d is the thickness of the crystal, n is the refractive index of the crystal at the wavelength of the probe beam, λ is the probe beam wavelength, γ_{41} is the EO coefficient, and E is the electric field of the THz wave. Thus, we can obtain the entire THz time-domain waveform by measuring the signal difference between I_x and I_y via a balance detector as a function of delay time between the THz pulse and the probe pulse. There are many different materials for EO sampling such as ZnTe, GaP, GaSe and InP. However ZnTe is now the most commonly used material for EO detection from sub-THz to several tens of THz, because of its relative large EO coefficient and good group velocity match. For high chopping frequency, EO sampling has a high SNR as well as photoconductive sampling, but it is more sensitive to laser noise.

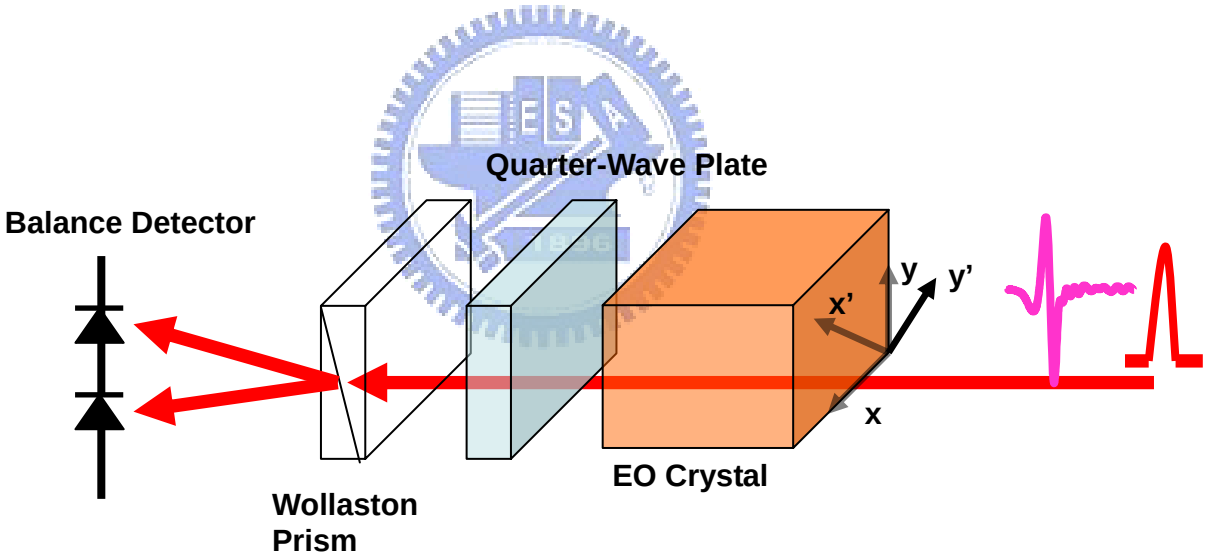

Fig.2-5 Schematic figure of Electro-optic sampling

2.3 Methods for Extraction of Optical Constants from THz-TDS

For THz time-domain spectroscopic (THz-TDS), both frequency dependent amplitude and phase information can be obtained by use of Fast Fourier Transform (FFT). Thus, we can use these information to extract the material's frequency dependent optical constants including complex refractive index and conductivity without use of Kramers-Kronig analysis. In this section we will discuss the electromagnetic theories and calculation methods for two different kinds of samples. First is to discuss how to deal with free standing thick sample which means the reflection signal in time domain can be clearly separated, and second we will discuss the method to solve the thin film sample case considering multiple reflections within it.

2.3.1 Thick Samples

If the measured sample is thick enough (typically >100 μm), the reflection signal in time domain is clearly separated. Thus, we can cut the reflection signal to simplify the analysis as shown in Fig. 2-6. The schematic figure of the electromagnetic model is shown as Fig. 2-7 assuming normal and plane wave incident, and the discussion is limited in frequency domain. $E_0(\omega)$ is the incident THz field, $E_{ref}(\omega)$ is the reference field (free space), and $E_{sample}(\omega)$ is the signal field transmitted through the sample. $\tilde{n}_1 = 1$ and $\tilde{n}_2 = n_2 + ik_2$ are refractive index for air and measured material. d is the thickness of sample and c is speed of light. The reference $E_{ref}(\omega)$ and signal $E_{sample}(\omega)$ field can be expressed by

$$E_{ref}(\omega) = E_0(\omega)e^{i\frac{\omega d}{c}}$$
$$E_{sample}(\omega) = E_0(\omega)e^{i\frac{n_2\omega d}{c}}e^{-\frac{k_2\omega d}{c}}t_{12}t_{21} \quad (2\text{-}16)$$

Where t_{12} and t_{21} are the Fresnel transmission coefficient, and can be expressed by

$$t_{12} = \frac{2}{1+\tilde{n}_2}$$
$$t_{21} = \frac{2\tilde{n}_2}{1+\tilde{n}_2} \tag{2-17}$$

From Eq (2-16) and Eq (2-17), the complex transmittance, $T(\omega)$, of the sample can be represented by

$$\tilde{T}(\omega) = \frac{E_{sample}(\omega)}{E_{ref}(\omega)} = \rho e^{i\Delta\phi} = e^{i\frac{(n_2-1)\omega d}{c}} e^{-\frac{k_2\omega d}{c}} \frac{4\tilde{n}_2}{(1+\tilde{n}_2)^2} \tag{2-18}$$

Both ρ and $\Delta\phi$ can be obtained from the Fourier transformed reference and signal THz pulses. If k_2 is much smaller than n_2 ($n_2 \gg k_2$), we could ignore the influence of k_2 in Eq (2-17), and thus the real part refractive index can be deduced directly from the phase difference in Eq (2-18) as represented by

$$n_2(\omega) = \frac{c\Delta\phi}{\omega d} + 1 \tag{2-19}$$

By substituting Eq (2-19) for Eq (2-18), the extinction coefficient, k_2, also can be obtained

$$\kappa_2 = -\frac{c}{\omega d} \ln \frac{\rho(1+n_2)^2}{4n_2} \tag{2-20}$$

From above calculation, we have the frequency dependent complex refractive index.

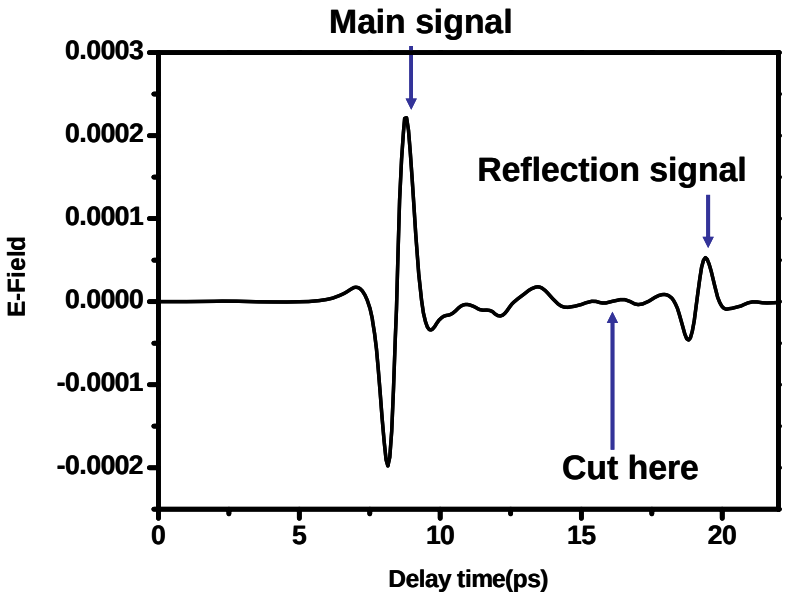

Fig.2-6 THz time-domain waveform transmitted a 470-μm-thick silicon, and the reflection signal is clearly separated from the main signal

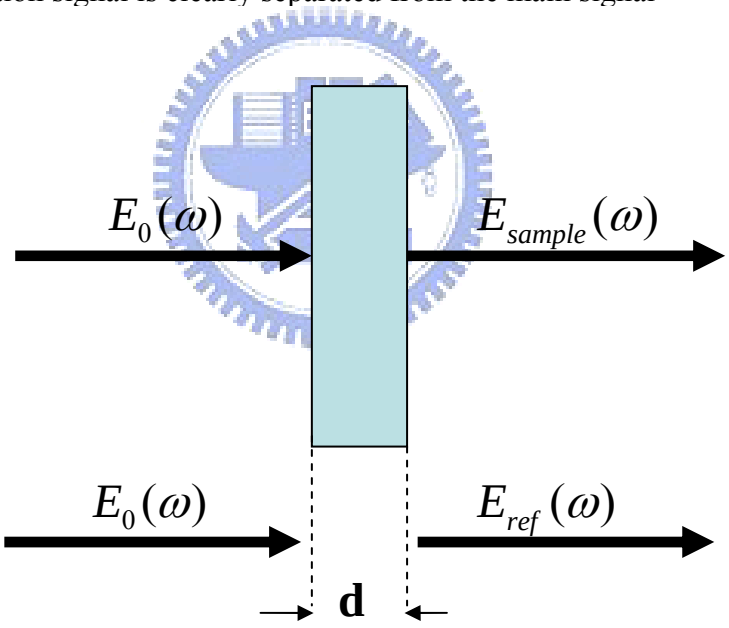

Fig.2-7 Schematic figure of electromagnetic model for thick sample

2.3.2 Thin Film Samples

Unlike method for thick sample discussed above, if the thickness of the measured sample was only several micrometers or even several hundred nanometers, the reflection signal couldn't be clearly separated in time-domain as shown in Fig. 2-8.

Thus, we have to take the multiple reflections within the thin film into consideration. The schematic figure of the electromagnetic model is shown in Fig. 2-9. $E_0(\omega)$ is the incident THz field, $E_{ref}(\omega)$ is the reference field (substrate only), and $E_{film}(\omega)$ is the signal field transmitted through the thin film. $\tilde{n}_1 = 1$, $\tilde{n}_2 = n_2 + ik_2$, and n_3 are refractive index for air, thin film and substrate, respectively. d is the thickness of the thin film and c is speed of light. $E_{ref}(\omega)$ can be determined by

$$E_{ref}(\omega) = t_{13}E_0(\omega)e^{i\frac{\omega d}{c}} \tag{2-21}$$

By considering the multiple reflections within the thin film, $E_{film}(\omega)$ can be represented by

$$E_{film}(\omega) = E_0(\omega)t_{12}t_{23}e^{i\frac{\tilde{n}_2\omega d}{c}} + E_0(\omega)t_{12}t_{23}r_{21}r_{23}e^{i\frac{3\tilde{n}_2\omega d}{c}} + E_0(\omega)t_{12}t_{23}r^2{}_{21}r^2{}_{23}e^{i\frac{5\tilde{n}_2\omega d}{c}}$$
$$+ \ldots\ldots\ldots\ldots + E_0(\omega)t_{12}t_{23}r^q{}_{21}r^q{}_{23}e^{i\frac{(2q+1)\tilde{n}_2\omega d}{c}} \tag{2-22}$$

Where q is the number of multiple reflections, and t_{12}, t_{12}, t_{23}, r_{21} and r_{23} are Fresnel amplitude transmission and reflection coefficients which can be expressed by

$$t_{12} = \frac{2}{1+\tilde{n}_2} \quad t_{13} = \frac{2}{1+n_3} \quad t_{23} = \frac{2\tilde{n}_2}{n_3+\tilde{n}_2}$$

$$r_{21} = \frac{\tilde{n}_2 - 1}{\tilde{n}_2 + 1} \quad r_{23} = \frac{\tilde{n}_2 - n_3}{\tilde{n}_2 - n_3} \tag{2-23}$$

Assuming the number of multiple reflections is infinite ($q \to \infty$), Eq (2-22) can be simplified as

$$E_{film}(\omega) = E_0(\omega)\frac{t_{12}t_{23}e^{i\frac{\tilde{n}_2\omega d}{c}}}{1 - r_{21}r_{23}e^{i\frac{2\tilde{n}_2\omega d}{c}}} \tag{2-24}$$

From Eq (2-21), Eq (2-23) and Eq (2-24), the theoretical complex transmittance can

be determined by

$$\tilde{T}_{the}(\omega,\tilde{n}_2)=\frac{E_{film}(\omega)}{E_{ref}(\omega)}=\frac{t_{12}t_{23}e^{-\frac{\kappa_2\omega d}{c}}e^{i\frac{\omega(n_2-1)d}{c}}}{t_{13}(1-r_{21}r_{23}e^{-\frac{2\kappa_2\omega d}{c}}e^{i\frac{2n_2\omega d}{c}})} \tag{2-25}$$

From THz-TDS data, we can have the experimental complex transmittance $\tilde{T}_{\exp}(\omega,\tilde{n}_2)$, but obviously there doesn't exit an exact solution for the complex refractive index. Therefore, we have to use a numerical method to extract the refractive index. For this purpose, we define an error function:

$$\left|\tilde{T}_{\exp}(\omega,\tilde{n}_2)-\tilde{T}_{the}(\omega,\tilde{n}_2)\right|=Error(\omega,\tilde{n}_2) \tag{2-26}$$

At a selected frequency, ω, if there exists a complex refractive index, $\tilde{n}_2$, that make the error function closest to zero, we can extract that refractive index by use of mathematical program. We set a range of complex refractive index for calculation and extract the best one which makes the error function almost zero within them for each frequency to have the entire complex refractive index information. In this work, we use Labview 6 for all the simulation and calculation and the calculated results will be discussed in ch 5.

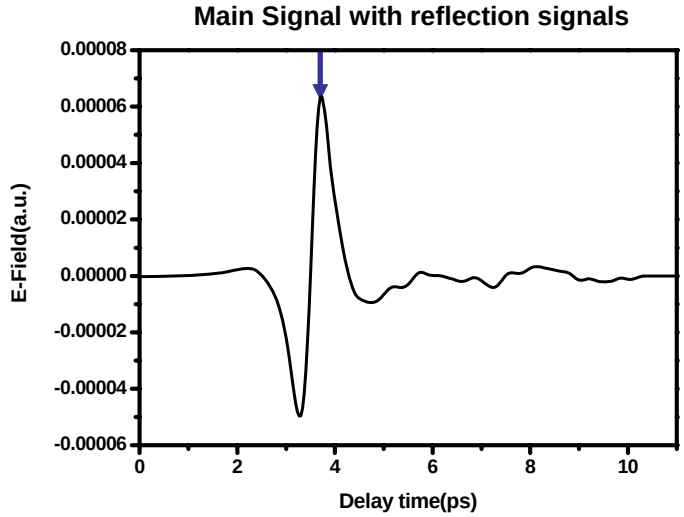

Fig.2-8 THz time-domain waveform transmitted through a 3-μm-thick GaN film. The reflection signals cannot be separated from the main signal.

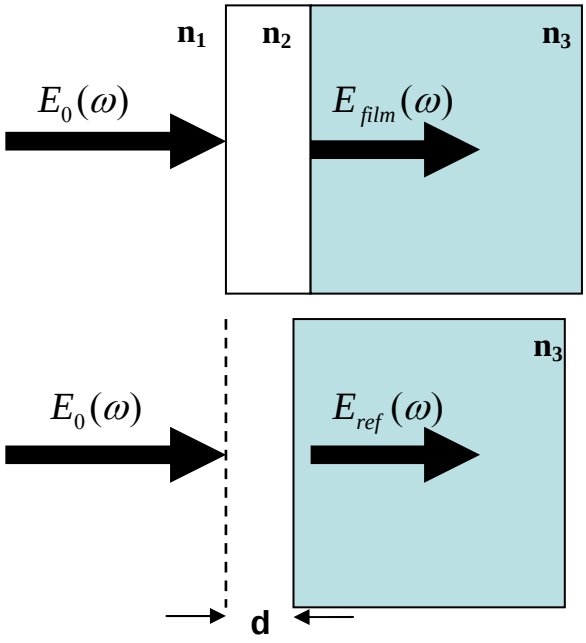

Fig.2-9 Schematic figure of electromagnetic model for thick sample

2.3.3 Optical Conductivity

From above calculations, we have the complex refractive index, and we can use it to obtain the complex conductivity of a conductor. First, we start from the Maxwell equation assuming a simple conducting medium with a flowing current, $\vec{J} = \sigma \vec{E}$, and the formula can be expressed by [21]:

$$\begin{aligned} \nabla \times \vec{H} &= \vec{J} + \frac{\partial \vec{D}}{\partial t} = \vec{J} - i\omega\varepsilon_0\varepsilon_\infty \vec{E} \\ &= -i\omega\varepsilon_0[\varepsilon_\infty - \frac{\sigma}{i\omega\varepsilon_0}]\vec{E} = -i\omega\varepsilon_0\varepsilon\vec{E} \\ \varepsilon &= \varepsilon_\infty + i\frac{\sigma}{\omega\varepsilon_0} \end{aligned} \qquad (2\text{-}27)$$

where ε_∞ is the contribution of the bound electrons and ε is the effective dielectric constant. We can have ε from the refractive index via the relation of $\varepsilon = (\varepsilon_r + i\varepsilon_i) = (n + i\kappa)^2$, and therefore the complex conductivity can be obtained

from Eq (2-27)

$$\begin{aligned}\sigma &= (\sigma_r + i\sigma_i) = i\omega\varepsilon_0(\varepsilon_\infty - \varepsilon)\\ \sigma_r &= \omega\varepsilon_0\varepsilon_i\\ \sigma_i &= \omega\varepsilon_0(\varepsilon_\infty - \varepsilon_r)\end{aligned} \tag{2-28}$$

The conduction of electrons in simple metals can be describe by a classical simple Drude model [22] which treat the free carriers in a solid as classical point charges subject to random collisions denoted as

$$\begin{aligned}\sigma(\omega) &= \sigma_r + i\sigma_i = \frac{\varepsilon_0\omega_p^2\tau_0}{1 - i\omega\tau_0}\\ \sigma_r(\omega) &= \frac{\varepsilon_0\omega_p^2\tau_0}{1 + \omega^2\tau_0^2}\\ \sigma_i(\omega) &= \frac{\omega\varepsilon_0\omega_p^2\tau^2{}_0}{1 + \omega^2\tau_0^2}\end{aligned} \tag{2-29}$$

The plasma frequency is defined by $\omega_p^2 = Ne^2 \big/ (m^*\varepsilon)$ where N is carrier concentration, e is the electronic charge and m^* is the effective carrier mass, and τ_0 is carrier relaxation time. The DC conductivity is given by $\sigma_{DC} = eN\mu$ where $\mu = e\tau_0 \big/ m^*$ is the carrier mobility. The simple Drude model indicates that the velocity of carriers is damped with a time constant τ_0 and is randomized following each collision event. The conduction properties of many semiconductors [8] [9] in the terahertz region have been justified to follow the simple Drude model, but some nanostructured materials show deviations from it. Recently, Smith proposed a modified Drude model [23], which can explain the deviations from the simple Drude model for the nanostuctured materials [10] [12], particularly the negative values of imaginary part of conductivity. The complex conductivity in the Drude-Smith model is given by

$$\sigma(\omega) = \frac{\varepsilon_0 \omega_P^2 \tau_0}{1 - i\omega\tau_0}\left[1 + \frac{c}{1 - i\omega\tau_0}\right] \qquad (2\text{-}30)$$

where c is a parameter describing fraction of the electron's original velocity after scattering and vary between -1 and 1. In the simple Drude model, the momentum of carrier is randomized after each scattering event, but in the Drude-Smith model, carriers retain a fraction, c, of their initial velocity. In particular, $c = 0$ corresponds to the simple Drude conductivity and $c = -1$ means that carrier undergoes complete backscattering. The Drude-Smith model predicts a DC conductivity of $\sigma = eN\mu(1+c)$ and thus the reduced macroscopic DC mobility is given by $\mu_m = (1+c)\mu$.

3. Sample Properties

In this chapter, we describe the growth method and electric properties of GaN and InN samples studied in this work.

3.1 GaN

The GaN epitaxial film used in this study was grown by metal-organic chemical vapor deposition facility (EmcoreD75). The sample structure consisted of a 25-nm-thick GaN buffer layer first grown on the c-plane of a sapphire substrate, followed by a 3.0-μm-thick Si-doped GaN layer. Half of this sample was deposited thin Ni layer with a thickness of 80 $\mathring{A}$ directly on top of the GaN film using an electron-beam evaporation. It was subsequently rapid thermal annealing (RTA) under flowing N_2 at temperatures 800–900 ◦C for 1 min to form various nanometer-sized Ni clusters (nanomasks). Finally, this sample with Ni nano-masks was then etched by a planar type ICP-RIE system to form a nanorod structure on the top surface. The SEM image of GaN-NR in Fig. 3-1 exhibit a uniform height of about 250nm and radius of~100nm. The carrier concentration of $3.3\times10^{18}\,cm^{-3}$ and mobility of $260cm^2/Vs$ of GaN epilayer were obtained by Hall effect measurement.

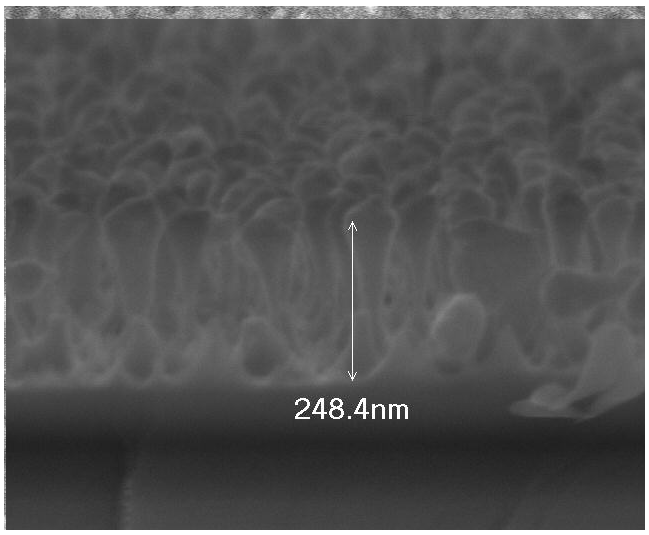

Fig. 3-1 SEM image of GaN-NR

3.2 InN

For this work, four InN samples were grown on Si (111) substrates by PAMBE. The InN epilayers were grown on Si(111) using the epitaxial AlN/β-Si_3N_4 double-buffer layer technique. Details of the growth procedure can be found elsewhere [24]. The InN nanorods were grown at sample temperature of 330°C (LT-NR) and 520°C (HT-NR) on -Si_3N_4/Si(111) (without the AlN buffer layer). The N/In flux ratios were ~ 2.6 and ~ 6.0 for LT-NR and HT-NR, respectively and were adjusted at different growth temperature to ensure that the growth proceeded in the columnar mode. The thicknesses of two InN epilayers, LT-NR, and HT-NR are ~ 1μm, 2.5 μm, 750 nm, and 700 nm, respectively. The morphologies and size distribution of InN nanorods were analyzed using field-emission scanning electron microscopy. The SEM image [25] of the hexagonal-shaped LT-NR in Fig. 1(a) exhibits nanorods with a uniform diameter of ~130 nm, while that of the HT-NR in Fig. 1(b) reveals that besides the large-size nanorods, there are ultra-small nanorods with an average diameter of ~60 nm filling up the spaces between larger-size (~ 130 nm) nanorods. The LT-NR exhibits an average aspect ratio (height/diameter) of ~ 6 and an aerial density of ~ 5×10^9 cm^{-2}. The average aspect ratio of the HT-NR is ~ 5.4 and ~ 12 for large and small nanorods, respectively and the aerial density of HT-NR is $8\times10^9 cm^{-2}$ including both modes. The electrical properties of each sample measured by Hall measurement are listed in Table. 3-1.

Sample	Thickness(μ m)	mobility(cm^2/Vs)	concentration(cm^{-3})
InN-epilayer (A)	1	1036	3.1×10^{18}
InN-epilayer (B)	2.5	1562	2.3×10^{18}
InN LT-NR	0.75	×	×
InN HT-NR	0.7	×	×

Table. 3-1 Thickness, Hall mobility and concentration of each InN sample.

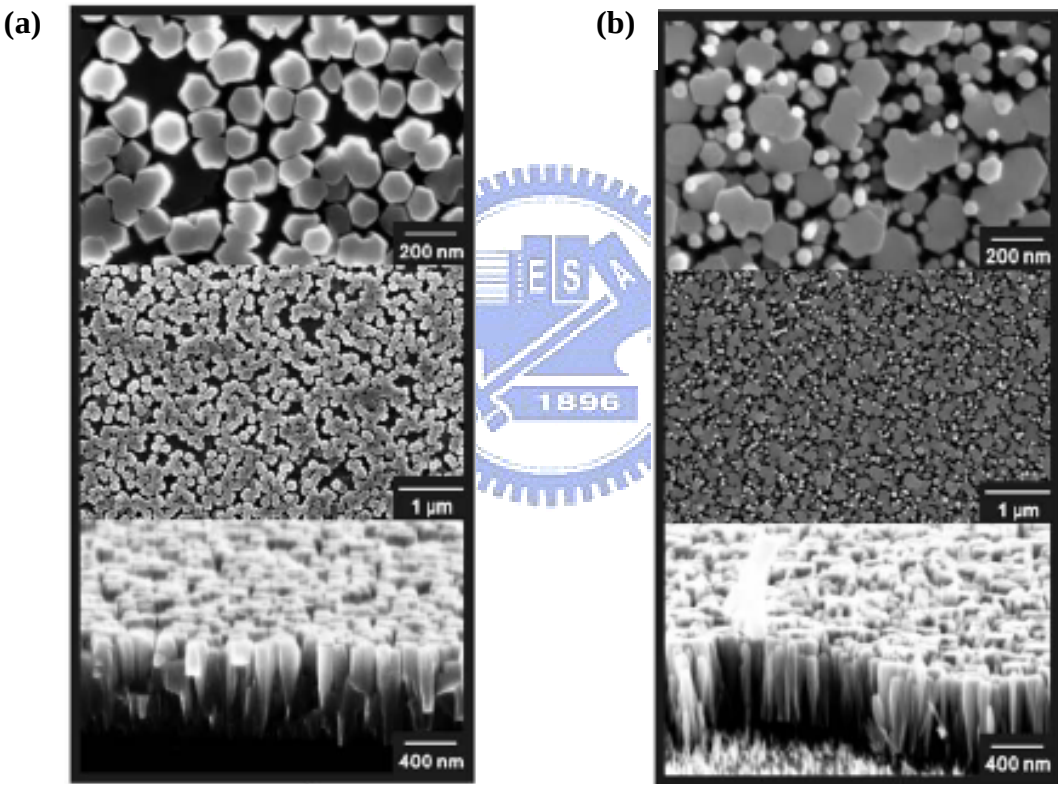

Fig. 3-2 SEM images of vertically aligned (a) low-temperature-grown nanorods (LT-NR) and (b) high-temperature-grown InN nanorods (HT-NR), grown on Si(111) substrates

4. Experimental Setups

In this chapter, we will describe the laser system and two different kinds of THz systems used in this work

4.1 Laser System

In this work, we use two different kinds of femtosecond laser systems (see Fig. 4-1). One of them is a oscillator titanium sapphire laser (Tsunami, Spectra-Physics) used as the seed laser; it is pumped by a frequency-doubled diode-pumped Nd:YLF laser at 532nm (Millennia V). Pumped with approximately 5W power, the titanium sapphire laser provides an output trace of intense 50fs pulses with wavelengths ranging from 750 nm to 850 nm (standard optics set). The pulse repetition rate is ~82MHz and the output power is up to 0.5 W. As an additional option, an 80ps operation mode (long-pulse operation) is available. The output beam of Tsunami is divided into two, one of them is used to drive the photoconductive THz system and the other is used as the seed laser directly guided into the regenerative laser system (Spitfire, Spectra-Physics).The seed laser is stretched to avoid damaging the amplifier crystal and a Q-switched intra-cavity frequency doubled (temperature-controlled LBO crystal) Nd:YLF lasers (Empower) is used to pump the amplifier at 527nm with repetition at 1kHz and power about 20W. The seed laser beam is resonated in the cavity and amplified about a million times. The amplified beam is then compressed to pulse width about 50fs and output. The amplification process is called chirped pulse amplification as shown in Fig 4-1. The spitfire provides an output trace of 50fs pulses with wavelength about 800nm.The repetition rate is 1 KHz and the output power is about 2W corresponding to 2mJ pulse energy.

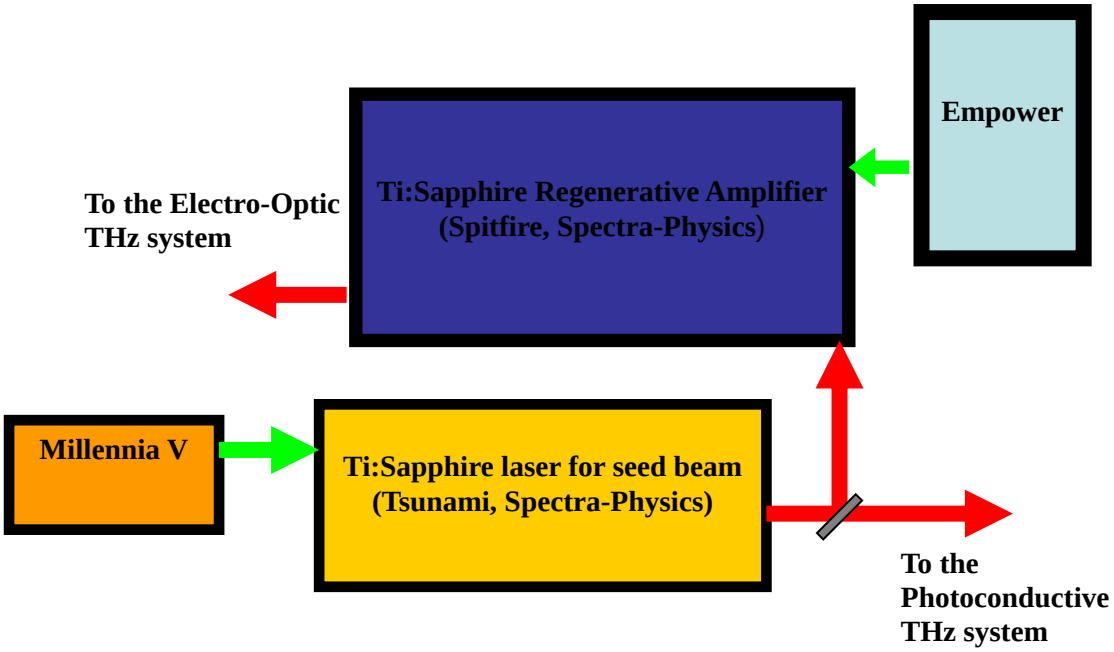

Fig.4-1 Femtosecond laser system includes Tsunami, Spitfire, and two pump laser (Millennia and Empower).

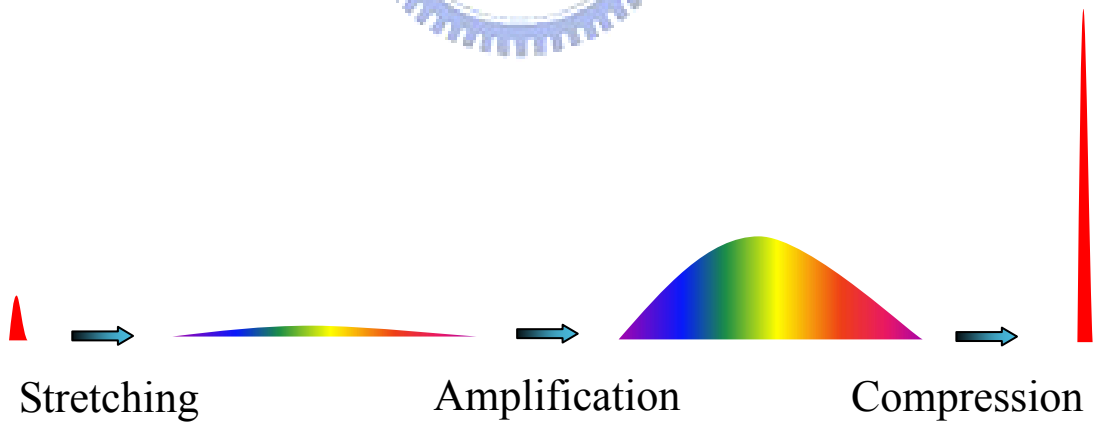

Fig.4-2 Schematic figure of chirped pulse amplification

4.2 THz Time-Domain Spectroscopy Setups

In this work, we use two different THz systems for different purposes. We use the photoconductive THz system to characterize optical constants of materials because of its high signal to noise ratio due to the high repetition rate of the driver laser. The other electro-optic THz system is driven by the amplified femtosecond laser system, and the high pulse energy can be used to excite the free carriers of materials for time-resolved study. The detail of two THz systems will be discussed below.

4.2.1 Photoconductive THz System

The schematic figure of the photoconductive THz system is shown in Fig. 4-3. An oscillator Ti:sapphire laser with central wavelength of 800nm at repetition of 82MHz is used. The laser beam is divided by a beam splitter into the pump beam and the probe beam, and both of them are focused onto the photoconductive antennas by two objective lenses to generate and detect the THz radiation. Here, the structure of the antenna is a dipole type Au/Ge/Ni coated electrode with a 5 μm gap deposited on a low temperature growth GaAs substrate (see Fig. 4-4). A 5volt AC bias with a frequency of 5kHz is applied to the emitter antenna to accelerate the carriers excited by the pump pulse by a function generator. Two hemispherical high resistivity silicon lenses connected to the substrates are used to collimate the THz radiation from the opposite side of the antenna substrates and also make the reflection signals from the substrates far away from the main signal. The generated THz radiation is collected and guided to transmit through sample or free space by a gold-coated off-axis parabolic mirror, and then the transmitted THz radiation is collected again and focused onto the detection antenna by another parabolic mirror. The focal lengths of both parabolic mirrors are three inches. A motor stage within the probe beam path is used to adjust the delay time between the pump pulse and the probe pulse. Thus, the

temporal profile of THz signal can be mapped out by monitoring the bias crossing the electrode of the detection antenna from a lock-in amplifier as a function of delay time between the pump pulse and the probe pulse. In order to avoid water vapor absorption, the entire THz beam path is located in a closed acrylic box which can be purged with nitrogen gas to decrease the environmental humidity. The THz time-domain waveforms and their corresponding spectrums of this system under different humidity are shown in Fig.4-5 and Fig. 4-6. The dips in the spectrum and the vibrations after the main peak in time-domain without nitrogen purge are because of the severe water vapor absorption, and obviously, the spectrum and the time-domain waveform become smoother by decreasing the humidity less than 5%. This system has a useful spectrum range from 0.2 to 2.5THz with a high signal to noise ratio (>10^6) that makes it suitable for characterization of static optical constants of materials.

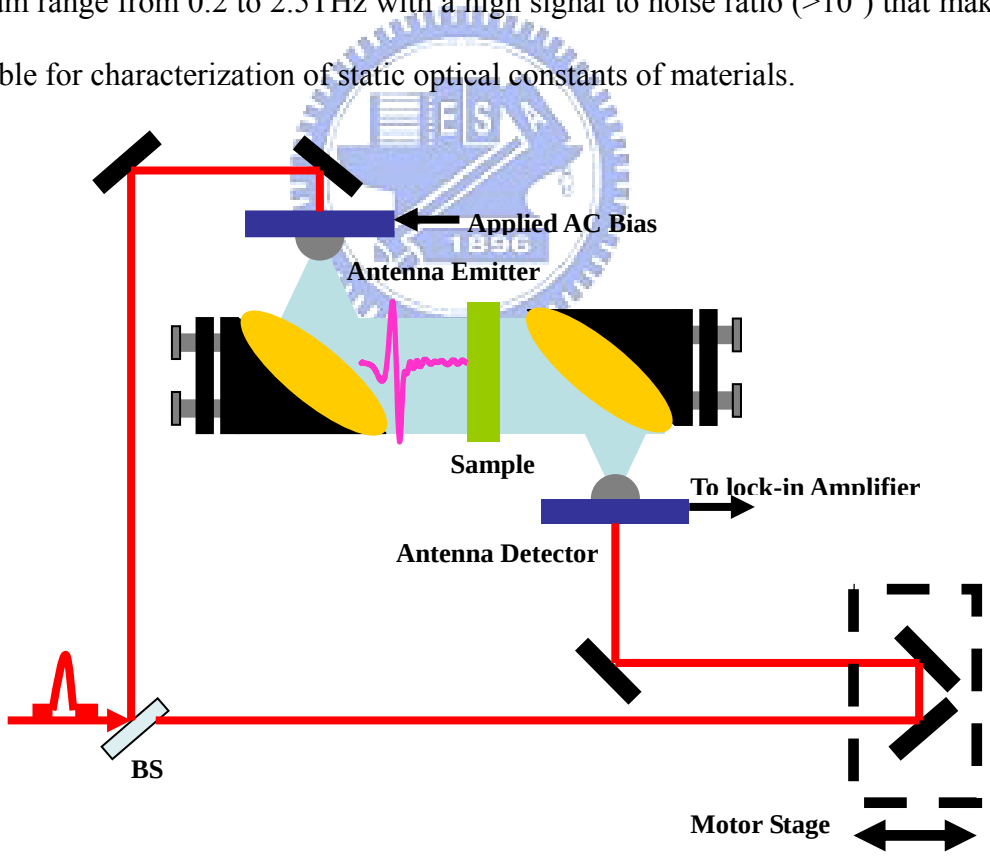

Fig.4-3 Setup of photoconductive THz system

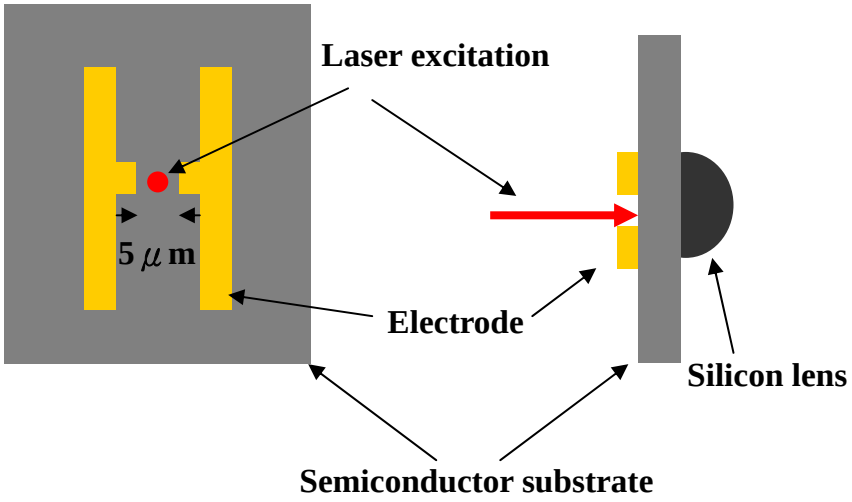

Fig.4-4 Structure of photoconductive antenna and silicon lens

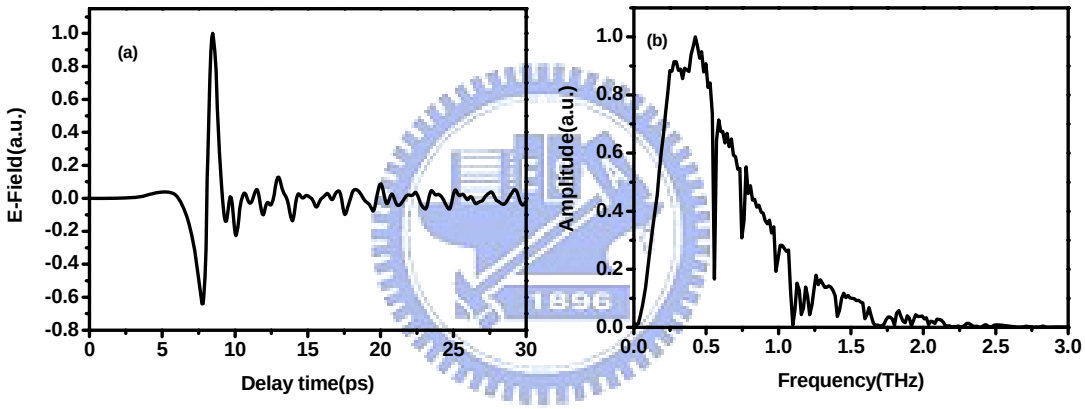

Fig.4-5 THz (a) time-domain waveform and (b) its corresponding amplitude spectrum under humidity of 55%

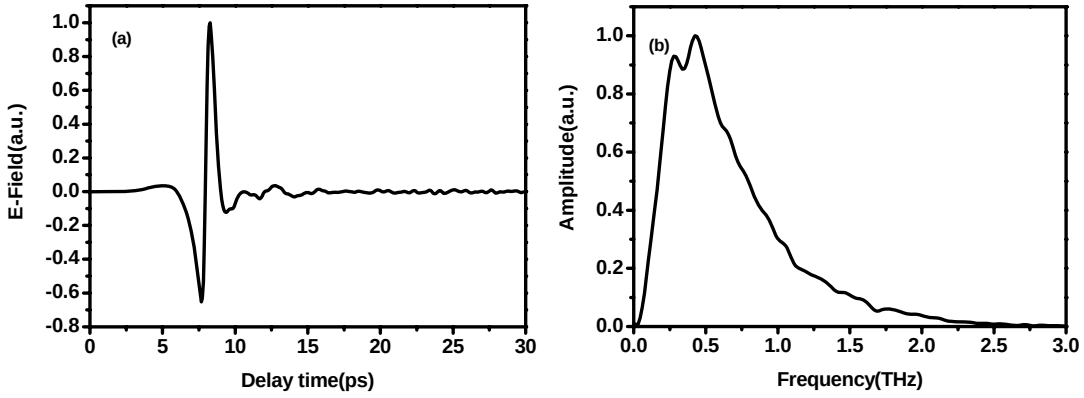

Fig.4-6 THz (a) time-domain waveform and (b) its corresponding amplitude spectrum under humidity of 5%

4.2.2 Electro-Optic THz System

The setup of the Electro-Optic THz system is shown in Fig. 4-7. An amplified Ti:sapphire laser providing 50fs, 800nm, 2mJ pulsed at repetition rate of 1kHz is used to drive this system. The linearly s-polarized incident beam is divided into three separated beams by two beam splitters. The transmitted beam from the first beam splitter is used for optical pump-terahertz probe study and will be discussed later. The reflected beam from the first beam splitter is divided into the pump beam and the probe beam by the second beam splitter. Polarization of the pump beam is rotated to linearly p-polarized by a half-wave plate and is the used to generate linearly p-polarized THz pulsed in a semiconductor surface emitter such as InAs at the incident angle of 70 degrees to the surface normal which is close to the Brewster angle. Any reflected laser beam from the emitter is blocked by a teflon sheet which has a high transmissivity in the terahertz region. The generated THz radiation is collimated and focused onto the sample by a pair of gold-coated off-axis parabolic mirrors with focal lengths of 3 and 6 inches respectively. The transmitted THz radiation is again collimated and focused onto a 2-mm-thick (110) ZnTe crystal for free space electro-optic sampling by another pair of parabolic mirrors with the same focal lengths with previous pair. A pellicle beam splitter which is transparent to the THz beam and has a reflectivity of 5% for 800nm light is used to make the probe beam collinear with the THz beam in the ZnTe crystal. The linear polarization of the probe beam is perpendicular to the polarization of the THz beam and we adjust the azimuth angle of the ZnTe crystal to achieve the highest modulation efficiency. The linear polarization of the probe beam without being modulated by the THz radiation is converted to circular polarization by a quarter-wave plate; Polarization of the probe beam modulated by the THz radiation is converted to ellipsoid polarization by a

quarter-wave plate. A Wollaston beam splitter is used to divide the modulated ellipsoid polarized probe beam into a linear s-polarized beam and a p-polarized beam. A balanced detector with two silicon photodiodes is used to detect the differential signal between two individual probe beams and the signal is proportional to the THz electric field. A motor stage within the probe beam path is used to scan the delay time between the probe pulse and the THz pulse imposing on the ZnTe crystal to obtain the entire THz time-domain waveform. In order to increase the signal to noise ratio, an optical chopper and a lock-in amplifier are used. The entire THz beam path is also located in a closed acrylic box for nitrogen purge. An example of a terahertz pulse with its corresponding spectrum under humidity of 5% generated by this setup is shown in Fig. 4-8.

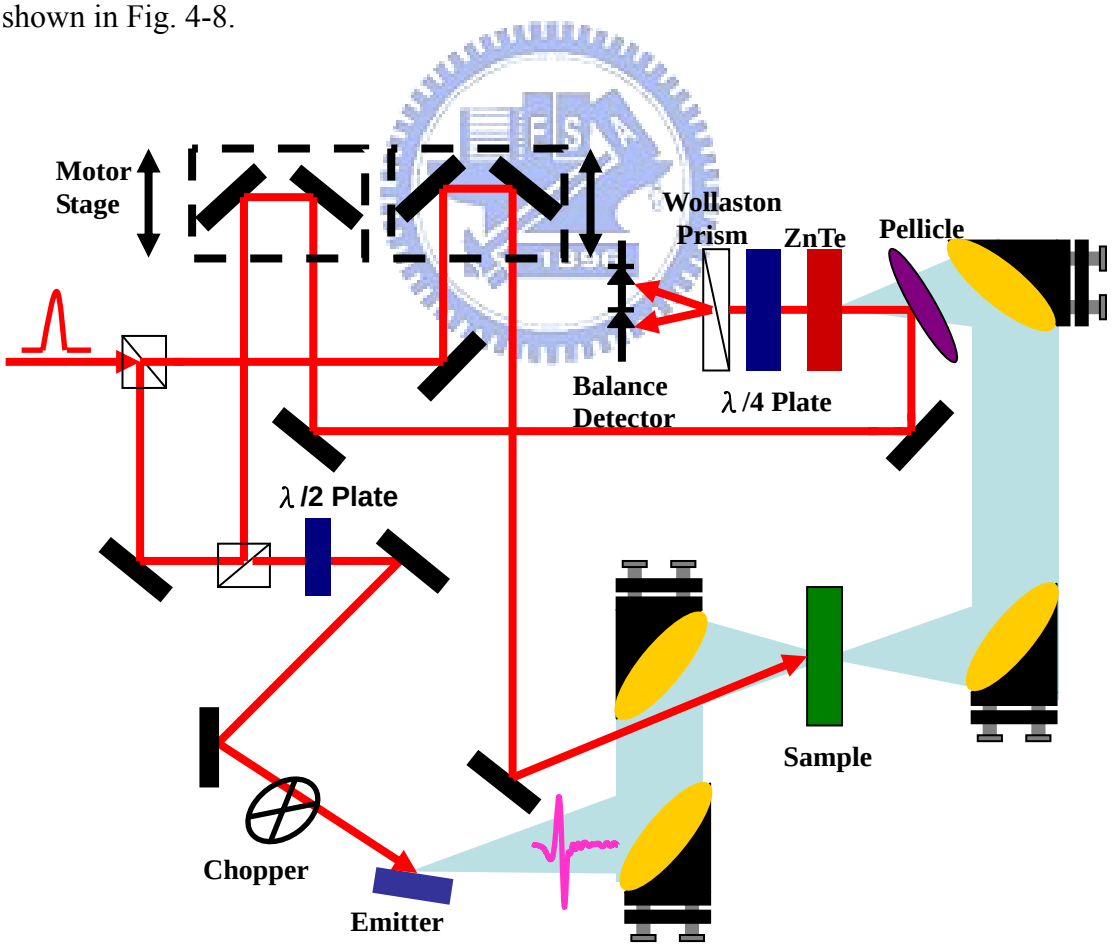

Fig.4-7 Electro-optic THz system

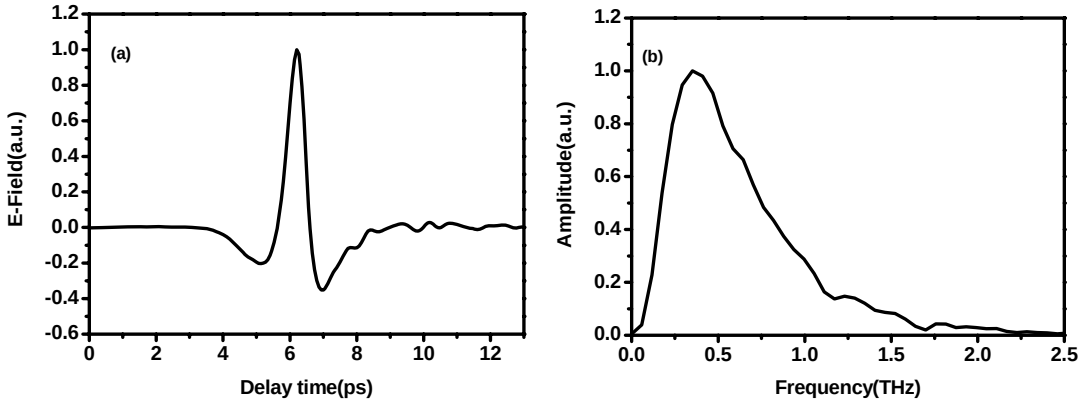

Fig.4-8 THz time-domain (a) waveform and (b) its corresponding spectrum generated by the electro-optic THz system using InAs as emitter under humidity of 5%

4.2.3 Optical Pump-Terahertz Probe (OPTP) System

OPTP is an ideal method for investigation of transient carrier dynamics. Although all optical pump-probe method provides superior time resolution in carrier relaxation study, the analysis is often difficult because the band filling effect and band gap renormalization may take place because of large incident photon energy. Thus, THz pulse with a small photon energy (4.1mev for 1 THz) which is far below the bandgaps of typical semiconductors can provide a more direct measure of conductivity and carrier transport in materials. The setup of OPTP in this work is based on the electro-optic THz system shown in Fig.4-7. The transmitted beam from the first beam splitter is guided to irradiate onto the sample at 5 degrees to the surface normal and a motor stage is used to scan the delay time between the THz pulse and the optical pump pulse. Thus, we can monitor the peak amplitude of the THz waveform in time-domain as a function of delay time between the THz pulse and the optical pump pulse (see Fig. 4-9), and because the excited carriers absorb the THz signal and the number of them decreases with time we can have the carrier relaxation information from the change of the THz peak amplitude.

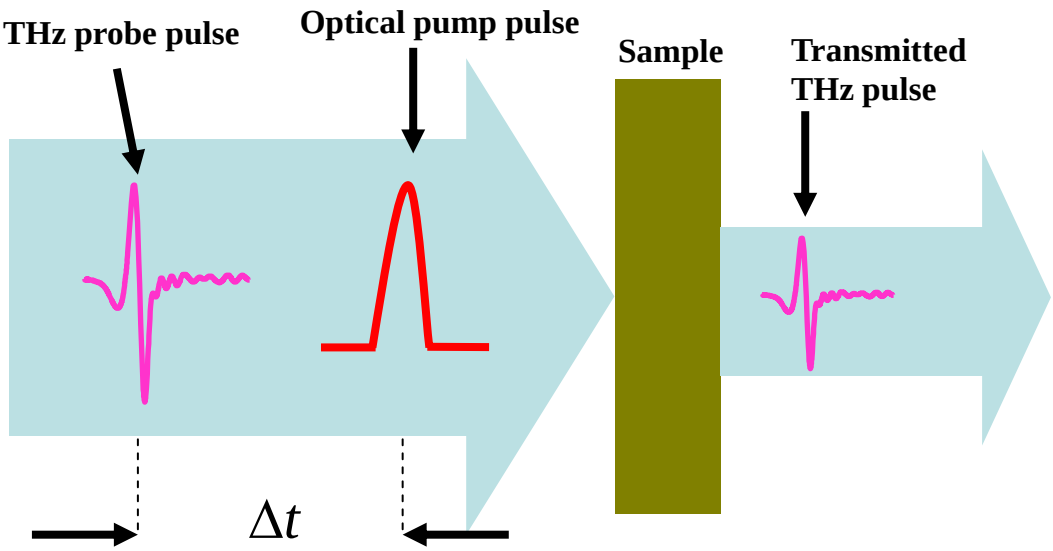

Fig.4-9 Schematic figure of OPTP

5. Experimental Results and Discussion

In this chapter, we first discuss the results of static optical properties of both GaN and InN samples measured by the photoconductive THz-TDS system and then we discuss the transient carrier dynamics of InN measured by optical pump-terahertz probe system. After characterizing the static and transient properties of InN samples, we will discuss characteristics of THz emission from InN eplayer and nanorods.

5.1 Static Optical Properties of GaN and InN

In this section we will discuss frequency dependent static optical properties of both GaN and InN samples measured by THz-TDS based on a photoconductive THz system as discussed in Chap 4

5.1.1 GaN

Prior to the measurement of the optical properties of the GaN samples, the accurate information of the refractive index of the substrates is required. The substrate of GaN film is a 430-μm-thick c-oriented sapphire. First, we put the bare sapphire substrate within the THz beam path and measure the transmitted THz signal. Figure 5-1 shows (a) THz time-domain waveforms with and without (free space) the sapphire substrate and (b) their corresponding amplitude spectrums and (c) the transmittance obtained via Fast Fourier Transform (FFT). The refractive index can be roughly calculated from the time shift of the THz waveform peaks in time domain from $(n-1)d/c = \Delta t$ to make sure the accuracy of later calculation. The time shift is about 2.935 ps and thus the roughly calculated refractive index is about 3.047. For precise calculation of the refractive index, Eq. (2-19) and Eq.(2-20) are used and the results are shown in Fig. 5-2. The frequency dependent refractive index of sapphire varies from 3.04 to 3.06 for 0.3 to 2THz, which is consistent with the previous results [8],

and the extinction coefficient is less than 0.02, so that we ignore it in later calculation.

Fig. 5-3 show (a) THz time-domain waveforms and (b) their corresponding spectrums transmitted through the 2.95 μm-thick n-type GaN thin film and sapphire substrate, and (c) the transmittance, which is about 20%. By use of the method discussed in section 2.3.2, the complex refractive index and conductivity were obtained. The calculated results are shown in Fig. 5-4. While real conductivity decreases as the frequency increases, imaginary conductivity slowly increases. This frequency dependence is typically observed for Drude-like material below the plasma frequency. Therefore, the measured complex refractive index and conductivity were then theoretically fitted using the simple Drude discussed in 2.3.3. The best fitting curves for the real part and imaginary part of refractive index and conductivity are also shown in Fig. 5-4. The fitting curves agree with the experimental data and two fitting parameters $\omega_p / 2\pi = 27.4 THz$ and $\tau_0 = 47\, fs$ were obtained. Assuming an electron effective mass $m^* = 0.22 m_0$ [26] for the GaN film, these fit parameters correspond to a carrier density $N = \omega_p^2 m^* \varepsilon_0 / e^2 = 2.1\times10^{18}$ cm^{-3} and a carrier mobility $\mu = e\tau_0 / m^* = 375$ cm^2/Vs, in reasonable agreement with room-temperature electrical Hall effect measurement result of 3.3×10^{18} cm^{-3} and 260 cm^2/Vs, respectively.

We have also measured the GaN-nanorod (GaN-NR) sample which is the same with the previous GaN sample but the top surface was etched to form a 250nm-height nanorods structure. Fig. 5-5 shows (a) the THz time-domain waveforms and (b) their corresponding spectrums transmitted through the GaN-NR sample and sapphire substrate, and (c) the transmittance. The transimittance of GaN-NR is about 25% which is slightly larger than previous GaN thin film. The calculated results of the

complex refractive index and conductivity using the same calculation parameters are shown in Fig. 5-6. The measured results are the effective phenomena including the top nanorods structure and the bottom GaN continuous film. In contrary to the previous GaN results (see Fig. 5-7), the slope of the real part conductivity increases, while the slope of the imaginary part conductivity decreases as the frequency increases. These phenomena are due to the geometrical properties of the nanorods structure and the frequency dependent responses cannot be well fitted by the simple Drude model. The detailed discussion on the THz response of non-Drude like optical properties of GaN-NR will be given in the next section.

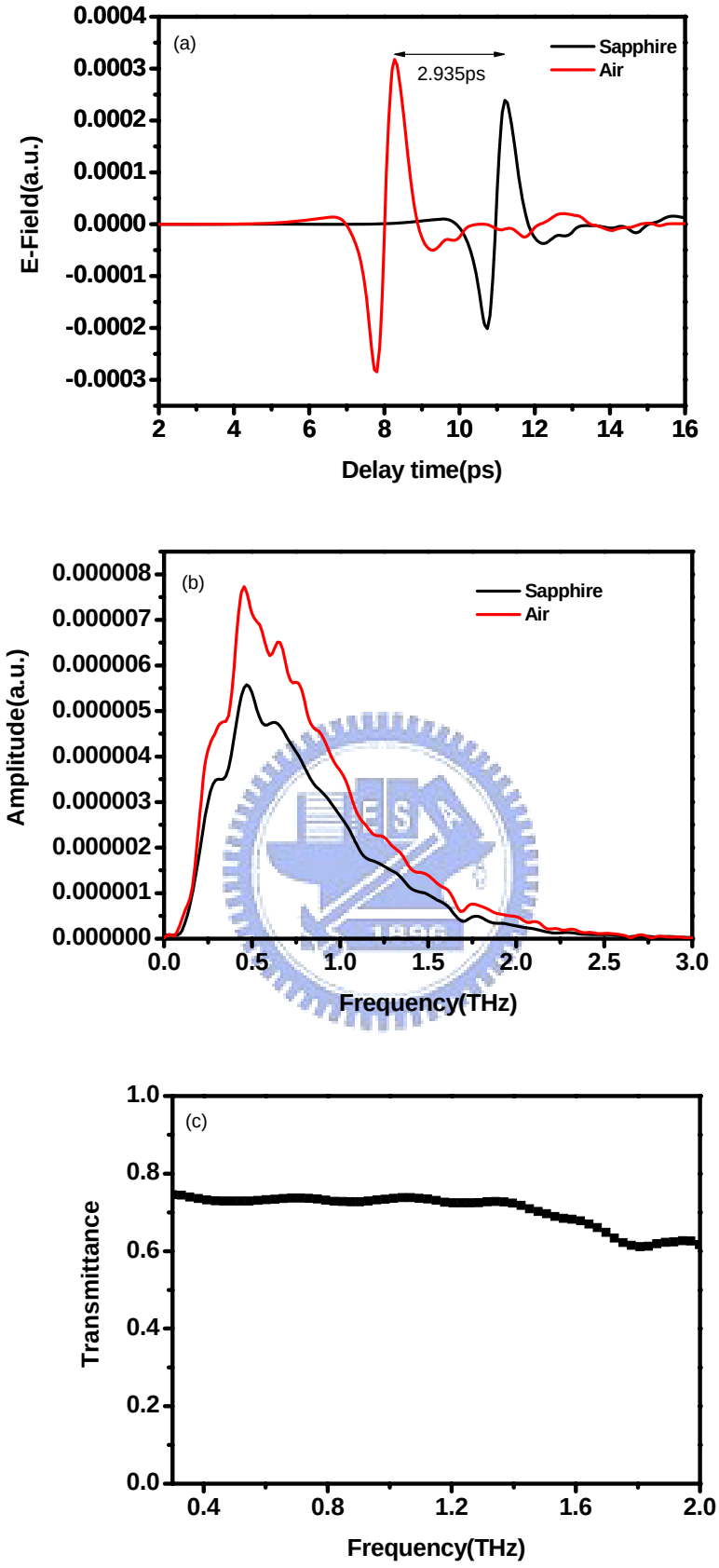

Fig.5-1 (a) THz time-domain waveform transmitted through sapphire and air, and (b) their corresponding amplitude spectrums. (c)The amplitude transmittance of sapphire

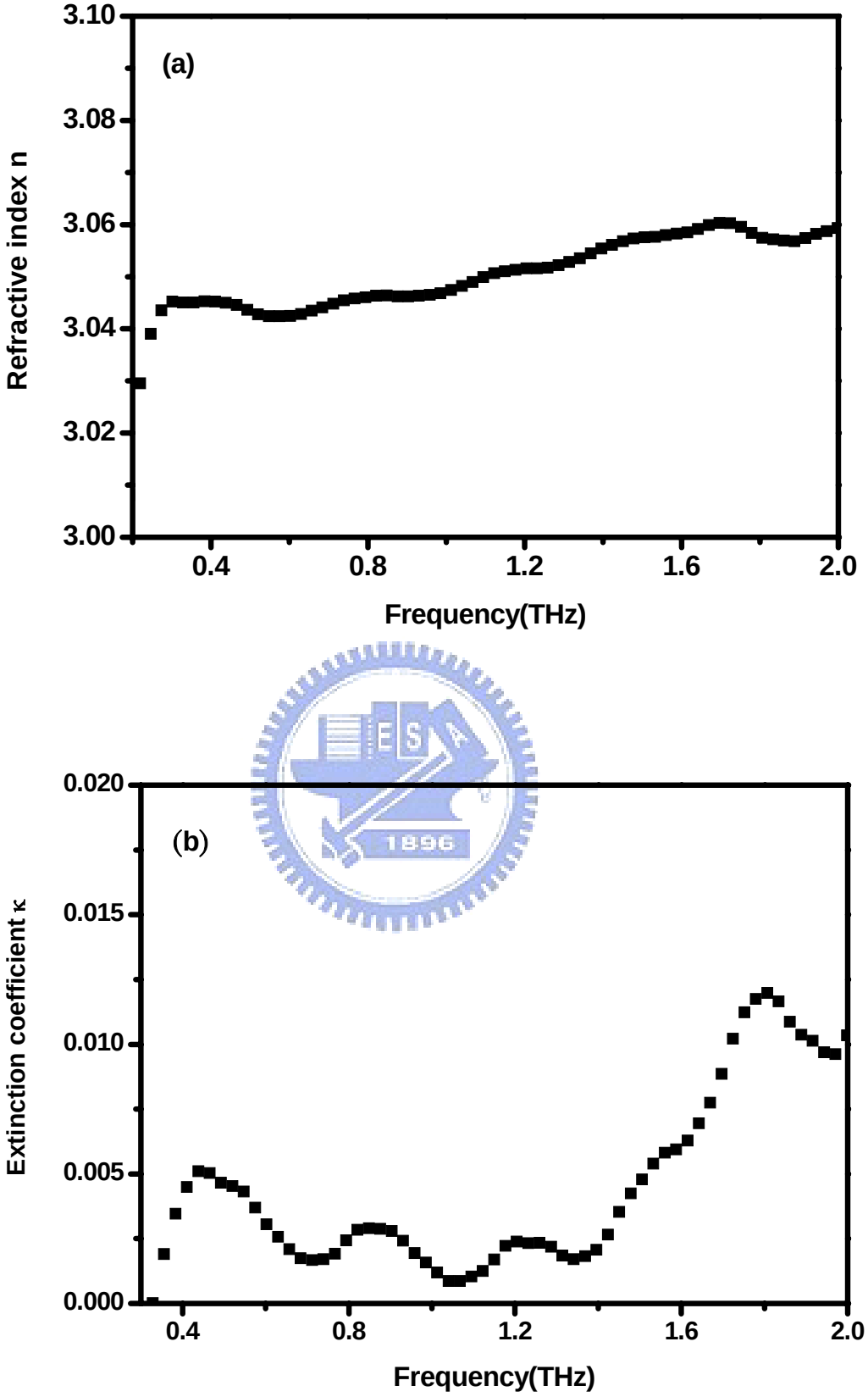

Fig.5-2 Frequency dependent (a) refractive index and (b) extinction coefficient of sapphire

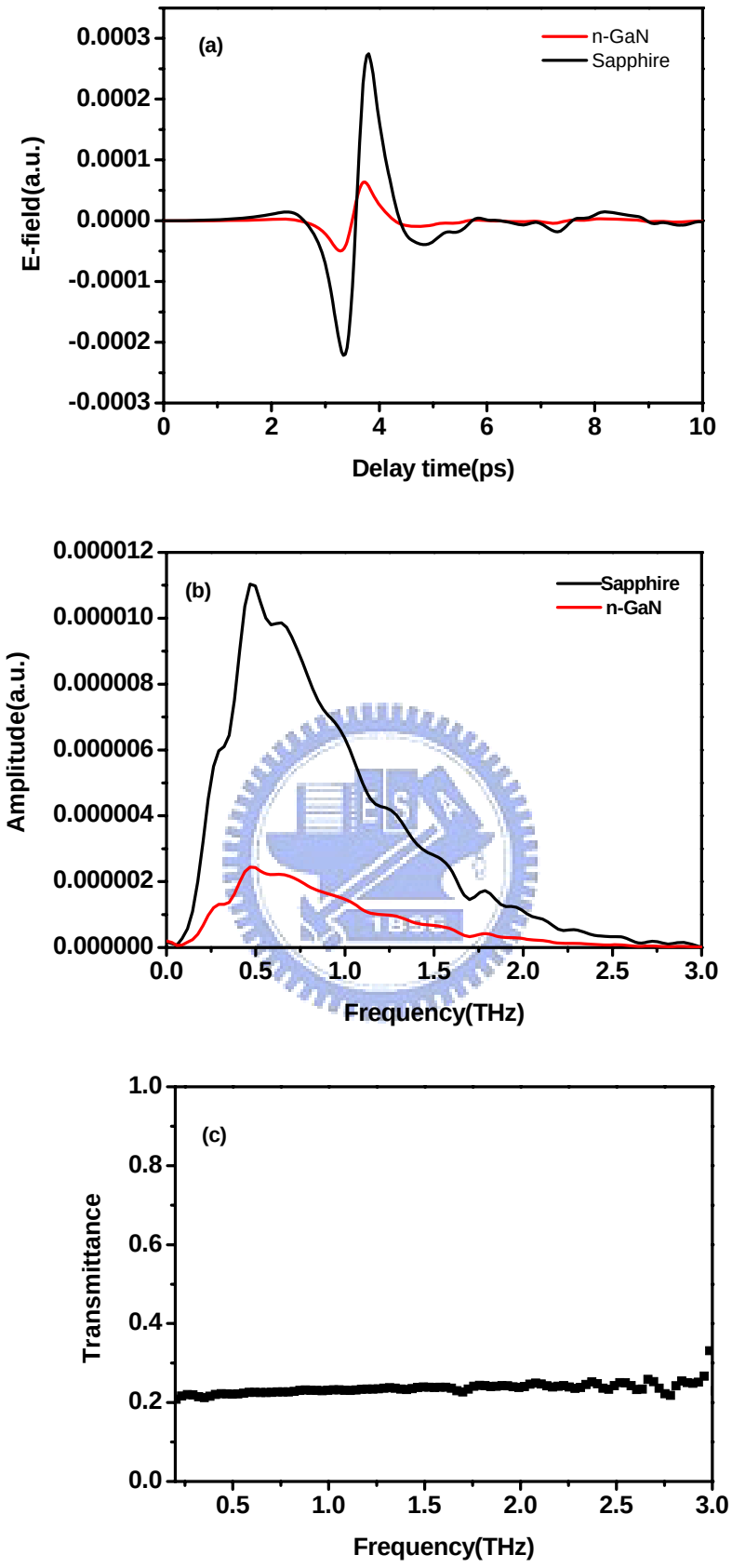

Fig.5-3 (a) THz time-domain waveform transmitted through n-GaN film and sapphire, and (b) their corresponding amplitude spectrums. (c)The amplitude transmittance of n-GaN film

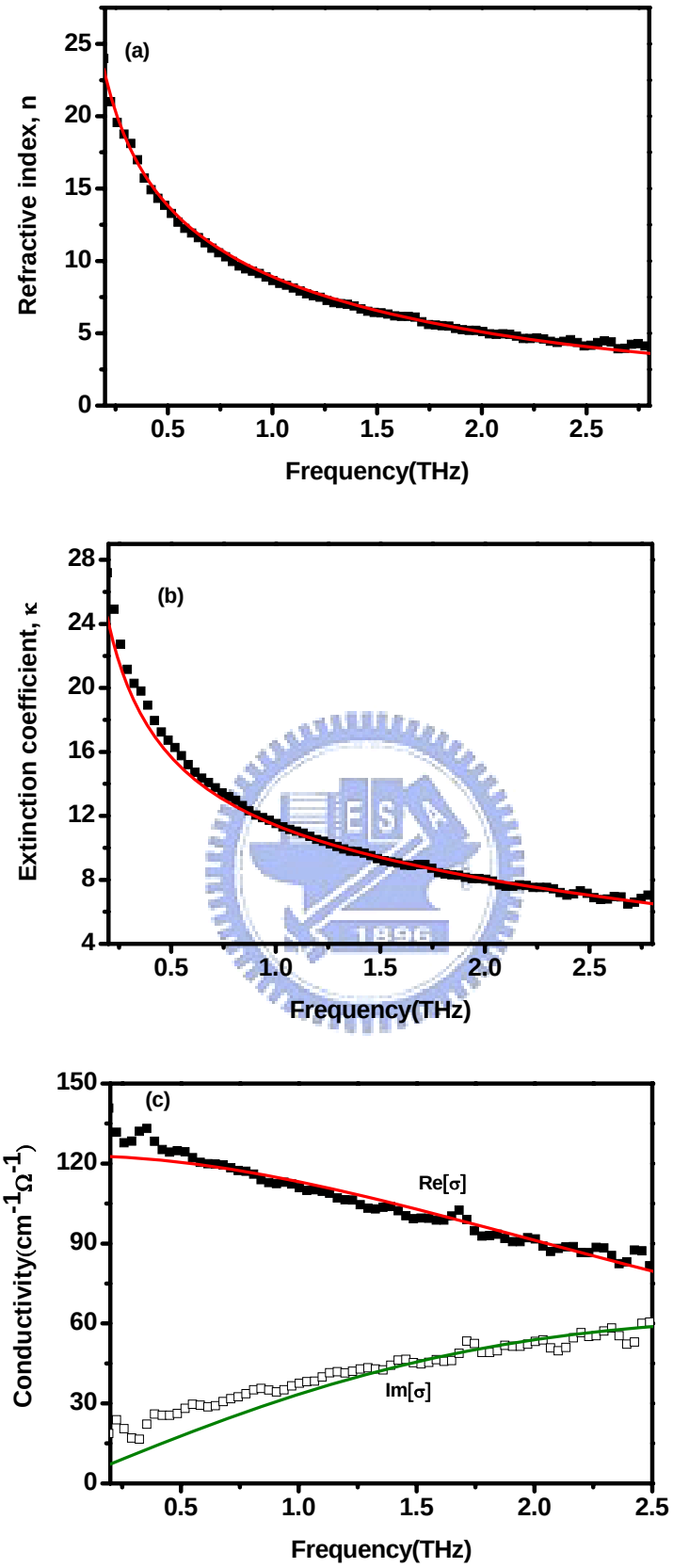

Fig.5-4 Experimental data (square) and fitting curves (solid line) of (a) refractive index, (b) extinction coefficient, and (c) complex conductivity of GaN film

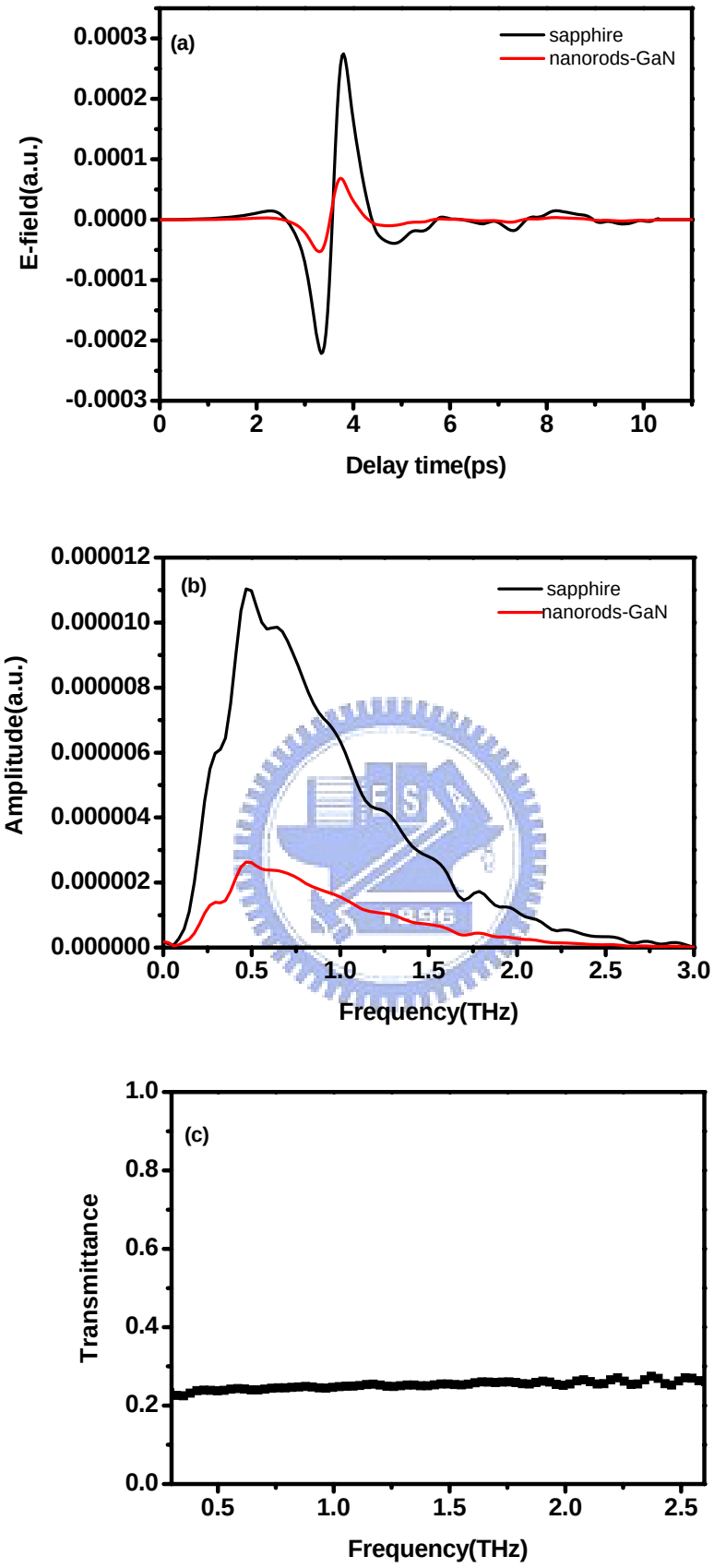

Fig.5-5 (a) THz time-domain waveform transmitted through GaN-NR and sapphire, and (b) their corresponding amplitude spectrums. (c)The amplitude transmittance of GaN-NR

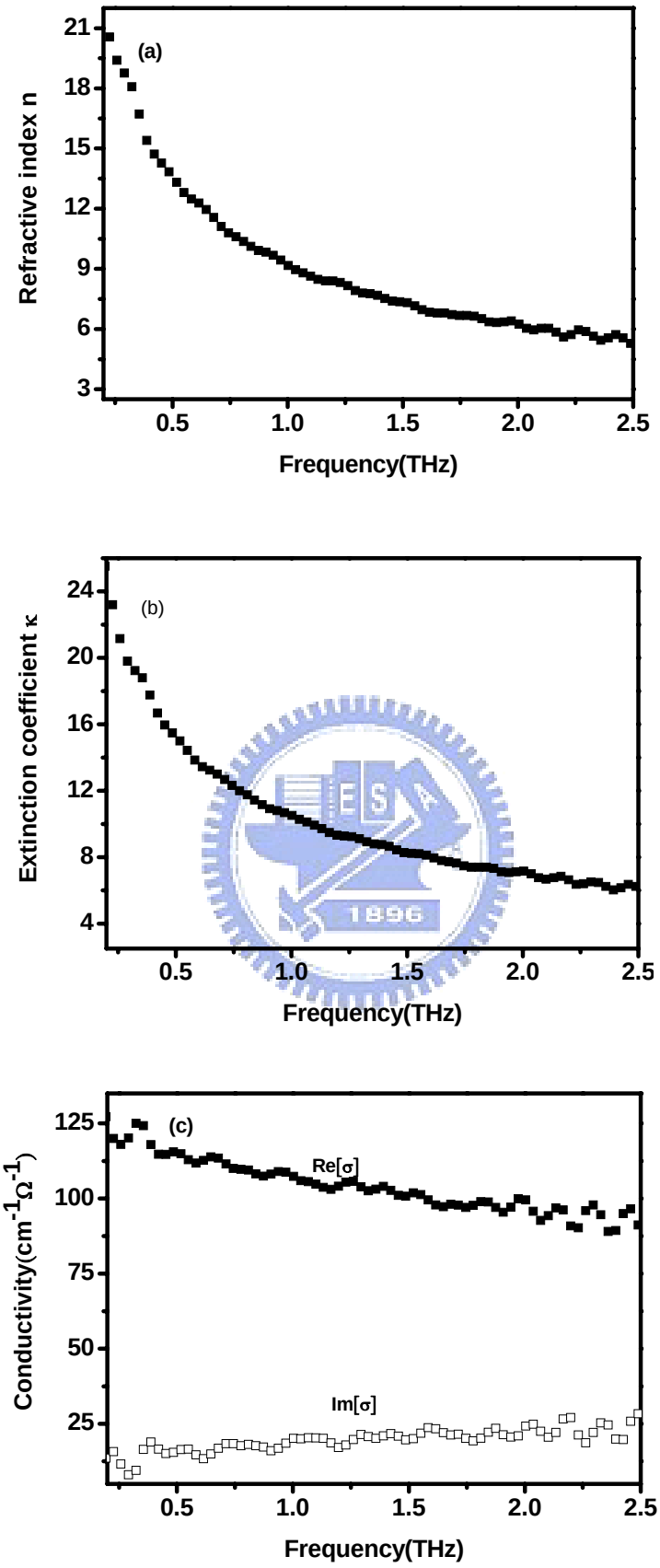

Fig.5-6 Experimental data and fitting curves of (a) refractive index, (b) extinction coefficient and (c) complex conductivity of GaN-NR

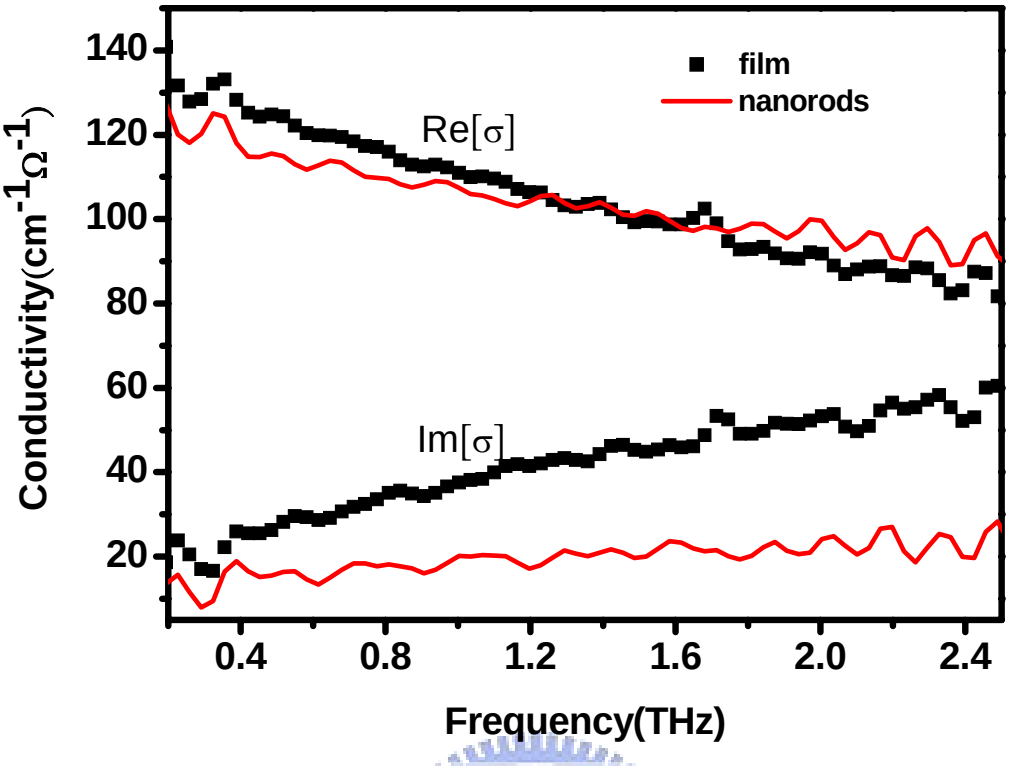

Fig.5-7 The complex conductivity of GaN with (solid line) and without (dot) nanorods

5.1.2 InN

First we have to determine the refractive index of the substrate. All the InN samples were grown on high resistivity (111) silicon substrates. Fig. 5-8 shows (a) the time-domain THz waveforms and (b) their corresponding amplitude spectrums transmitted through a 467- μm -thick silicon substrate and free space. The transmittance shown in Fig 5-8(c) varies from 60% to 80%. The time shift of the THz waveform peak is about 3.77ps and the corresponding rough refractive index is about 3.42. The precise results calculated by Eq (2-11) and Eq (2-12) are shown in Fig. 5-9, and the refractive index is 3.41 which is consistent with previous results [8] and the extinction coefficient is less than 0.05, so that we could ignore it for later calculation.

After determining the refractive index of the silicon substrate, we measured the InN samples. We first measured two InN epilayer samples (A and B) with different

thickness and carrier concentration. The THz time-domain waveforms and their corresponding spectrums transmitted through both samples and substrates are shown in Fig.5-10 and Fig. 5-12. The transmittance of sample A and B are about 20% and 6% respectively. The calculated complex refractive index and conductivity of both samples are shown in Fig. 5-11 and Fig. 5-13 respectively. The conductivities of both samples show the same behavior with the results of GaN thin film that the real part conductivity decreases with increasing frequency, while the imaginary part slowly increases. Thus both results were then theoretically fit using the simple Drude model. The best fitting curves are shown in Fig. 5-11 and Fig. 5-13, respectively and they agree well with experimental results. Two fitting parameters $\omega_p / 2\pi = 52,49THz$ and $\tau_0 = 52,70\,fs$ for sample A and B were obtained, respectively. Assuming $m^* = 0.075m_0$ for InN with carrier concentration about $3\times10^{18} cm^{-3}$, these fit parameters correspond to the carrier density $N = \omega_p{}^2 m^* \varepsilon_0 / e^2 = 2.5\times10^{18}$ and 2.2×10^{18} cm^{-3}, and the carrier mobility $\mu = e\tau_0 / m^* =$ 1217 and 1639cm^2/Vs for sample A and B, respectively, in reasonable agreement with room-temperature electrical Hall effect measurement result of 3.1×10^{18}, 2.3×10^{18}cm^{-3} and 1036, 1562 cm^2/Vs for sample A and B, respectively.

The THz time-domain waveforms and their corresponding spectrums transmitted through LT-NR and silicon substrate are shown in Fig. 5-14. The transmittance shown in Fig. 5-14(c) is about 25%. The measured refractive index is effective phenomena with contributions from both the air and the pure LT-NR. A simple effective medium theory [30] of $\varepsilon_{eff} = f\varepsilon_{rod} + (1-f)\varepsilon_{air}$ is employed to obtain the dielectric function of LT-NR, where f ~70% is filling factor of LR-NR. Fig. 5-15 shows the frequency-dependent (a) complex refractive index and (b) complex

conductivity of the LT-NR. The measured complex refractive index of LT-NR shows the similar monotonic decrease to InN-epilayer as the frequency increases. But the complex conductivity response is different from that of InN-epilayer. The real part conductivity gradually increases, while imaginary part conductivity with a negative value keeps decreasing as the frequency increases. This frequency dependence cannot be explained by the simple-Drude model, in which the frequency-dependent real conductivity should have a maximum at zero frequency and monotonically decrease, and the imaginary conductivity is always positive. As mentioned in section 2-3-3, this deviation, also observed in InP-NC [10] ZnO [11] and Si-NC [12], has been attributed to the backscattering of electrons at interface and surface or grain boundary.

We applied the Drude-Smith model to fit our experimental data and an excellent fit of complex refractive index and conductivity is obtained. The solid curves in Fig. 5-15 are obtained with the fit parameters c = –0.65, τ_0 = 13 fs, and $\omega_p/2\pi$ = 199 THz. The reduced DC electron mobility in the Drude-Smith model is given by $\mu_m = (1+c)(e\tau_0/m^*)$, which requires the exact value of the effective mass. But up to now no reported value of the effective mass of the InN nanorods is available in literatures. Recently, we have shown that vertically aligned InN nanorod arrays grown on silicon by PAMBE possess the crystal properties similar to wurtzite InN single crystal [27]. Therefore we assumed that the relation between N and m^* for the InN nanorods are similar to that for the InN single crystal. Using N = 1.5×10^{19} cm^{-3} calculated from the PL measurement as the carrier density of LT-NR, we obtained the corresponding effective mass of 0.1 m_0 from N vs. m^* relation calculated by the Kane's two-band ***kp*** model [28] and used it for later calculation. From the best fit parameters in the Drude-Smith model, an electron mobility of $80cm^2/Vs$ with an electron density of 4.9×10^{19} cm^{-3} is obtained, which is at the same order with PL

results. This agreement justifies our assumption that the effective mass of the InN-NR is similar to that of the InN epilayer.

A negative value of *c* for LT-NR reflects the localization of electrons within the nanorods and the long-range transport between nanorods is resctricted. Thus, the value of *c*, describing the event of scattering, is sensitive to scattering off at the boundaries and surfaces of nanostructures, therefore to the size of the nanostructures. The value of $c = -0.65$ for InN nanorods is bigger than those of a few nm-diameter nanostructures, which is typically nearly –1. This indicates that electrons within the InN nanorods with the diameter of ~ 130 nm are still highly mobile for long enough distances before they are bounced off from the boundaries of the rods. The separation distances between the InN nanorods are wide and some of them are of the order of the nanorods. Therefore, inter-rod transport due to the electronic coupling between isolated nanorods may be severely prohibited and consequently the observed mobility in the InN nanorods is mainly attributed to the intra-rod transport of electrons.

We have successfully used Drude-Smith model to describe the conduction properties of InN nanorods, but for GaN-NR case, the results cannot fit both simple Drude and Drude-Smith model because the results include both phenomena of top nanorods structure and bottom continues film that make this problem more complicated. Nevertheless, the deviations of conductivity are toward to Drude-Smith model from simple Drude model and thus we can predict that the nanorods structures on the top surface also follow the Drude-Smith model.

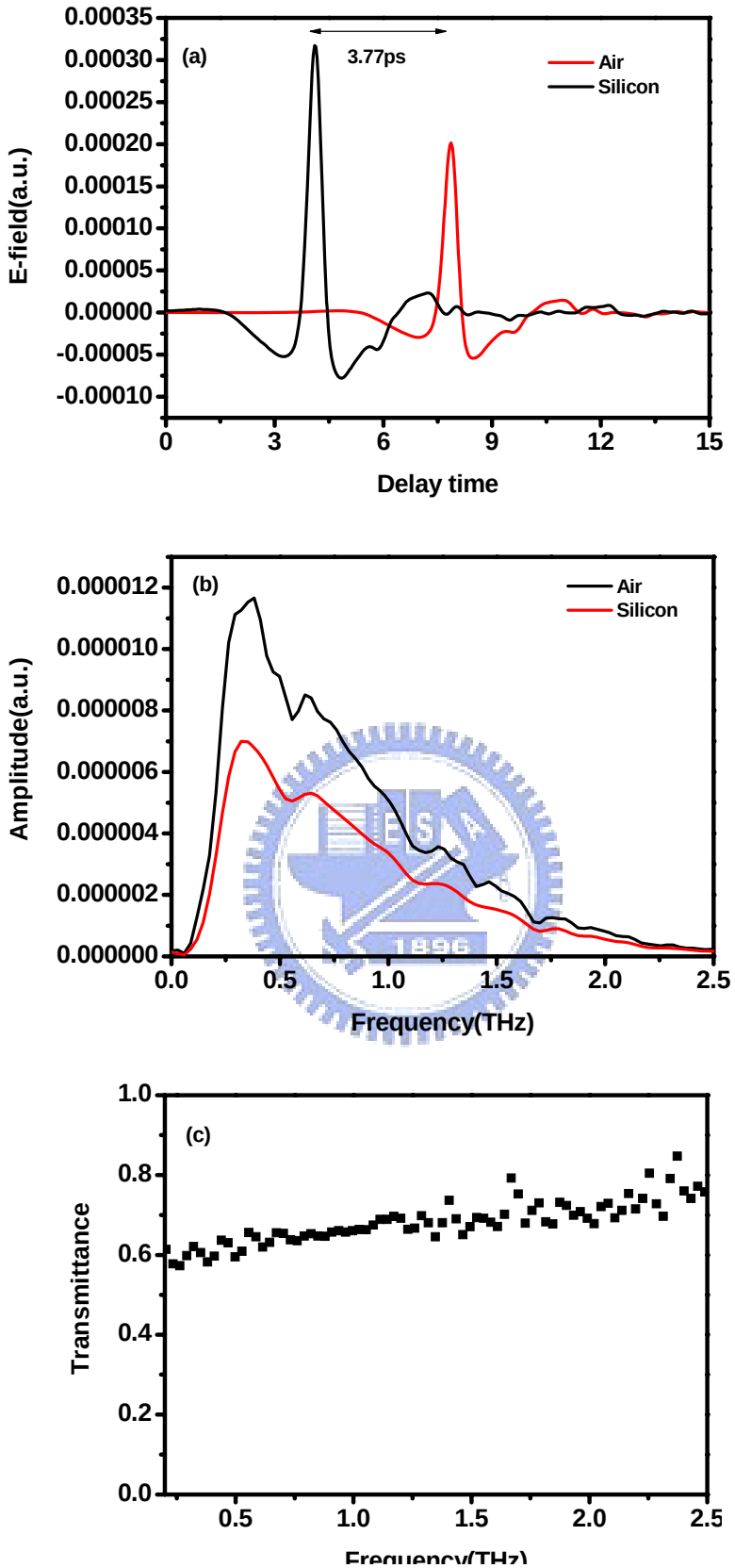

Fig.5-8 (a) THz time-domain waveform transmitted through silicon substrate and free space, and (b) their corresponding Amplitude spectrums. (c) The amplitude transmittance of the silicon substrate.

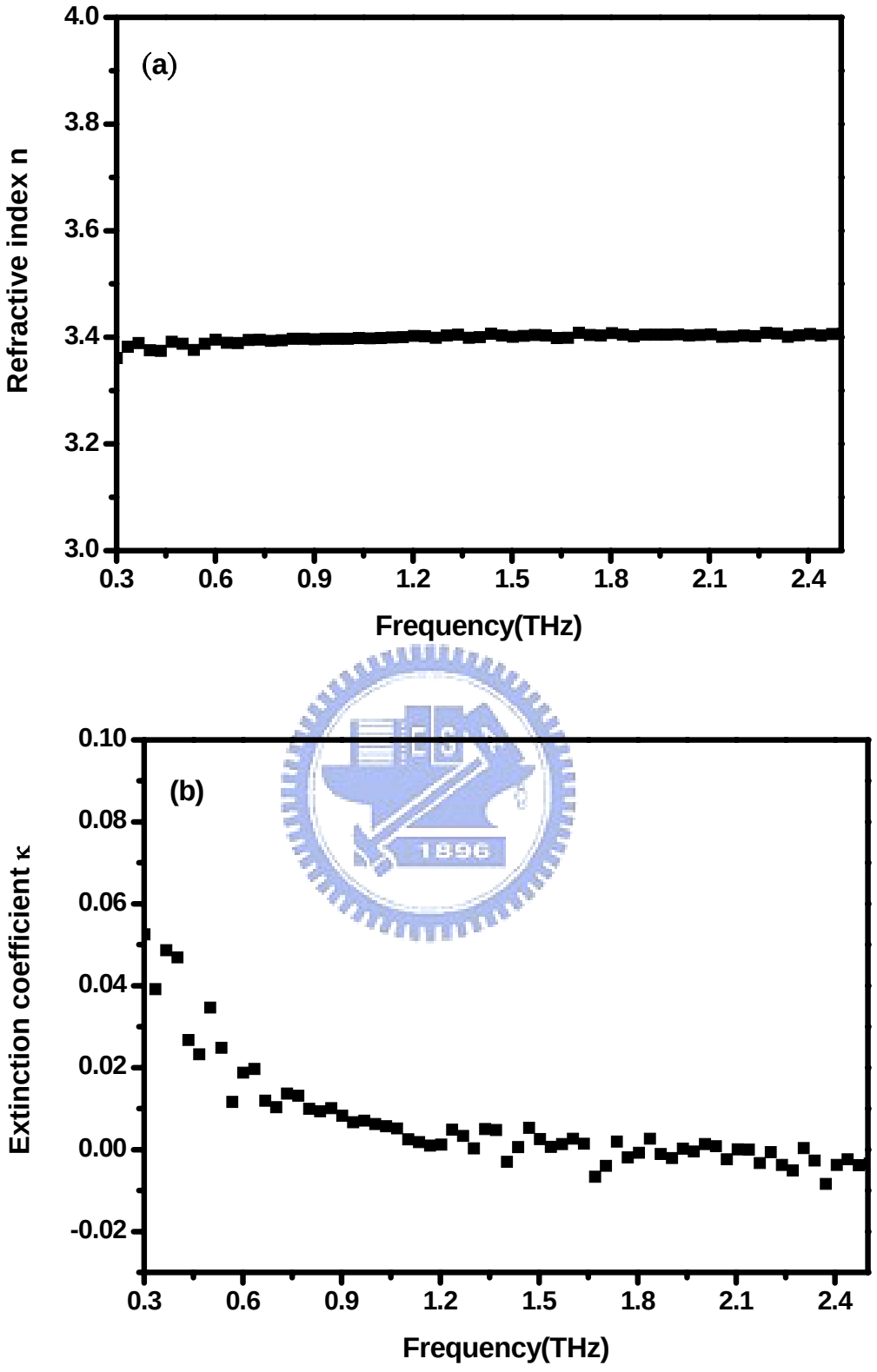

Fig.5-9 Frequency dependent (a) refractive index and (b) extinction coefficient of silicon substrate

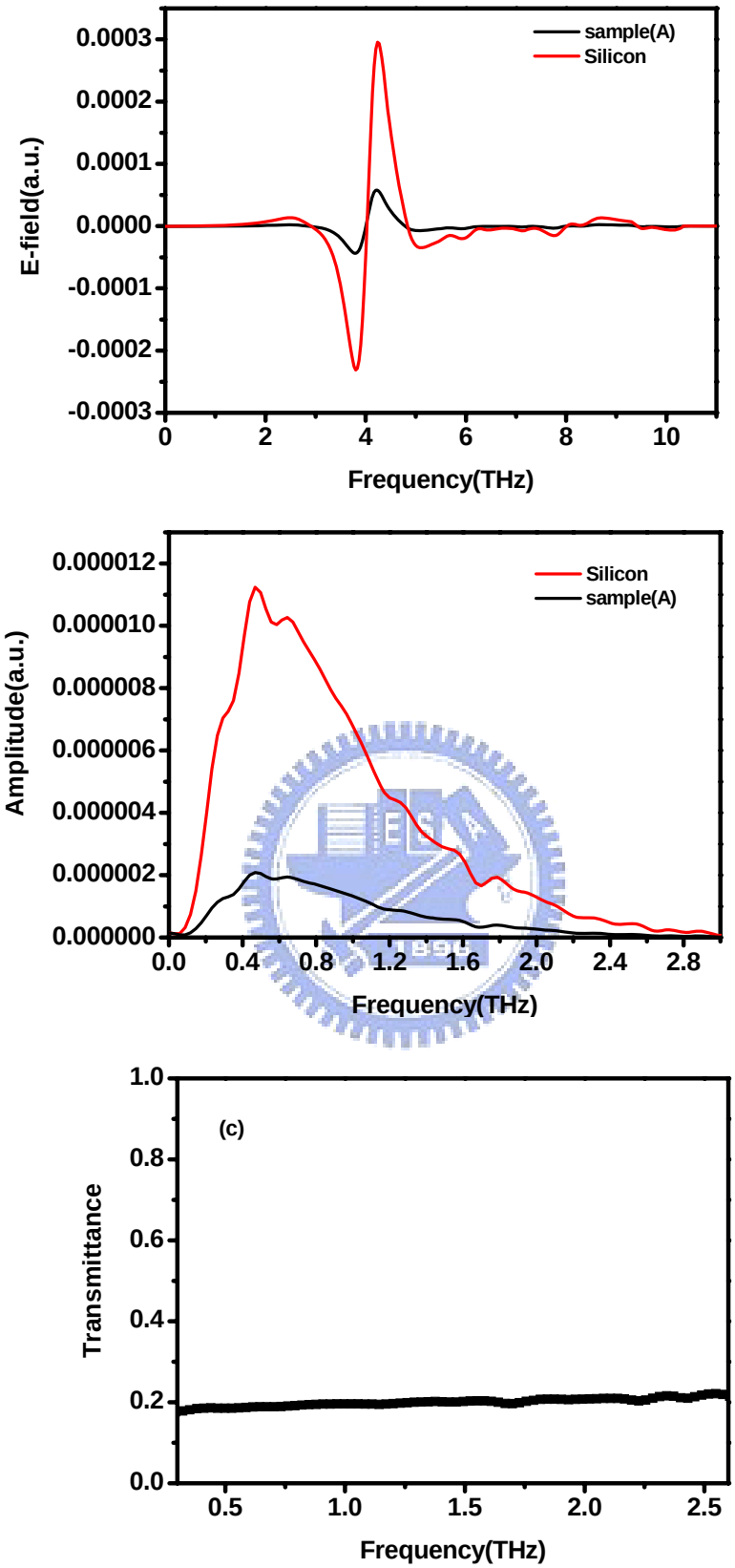

Fig.5-10 (a) THz time-domain waveforms transmitted through InN sample (A) and silicon substrate, and (b) their corresponding Amplitude spectrums. (c) The amplitude transmittance of the InN sample (A).

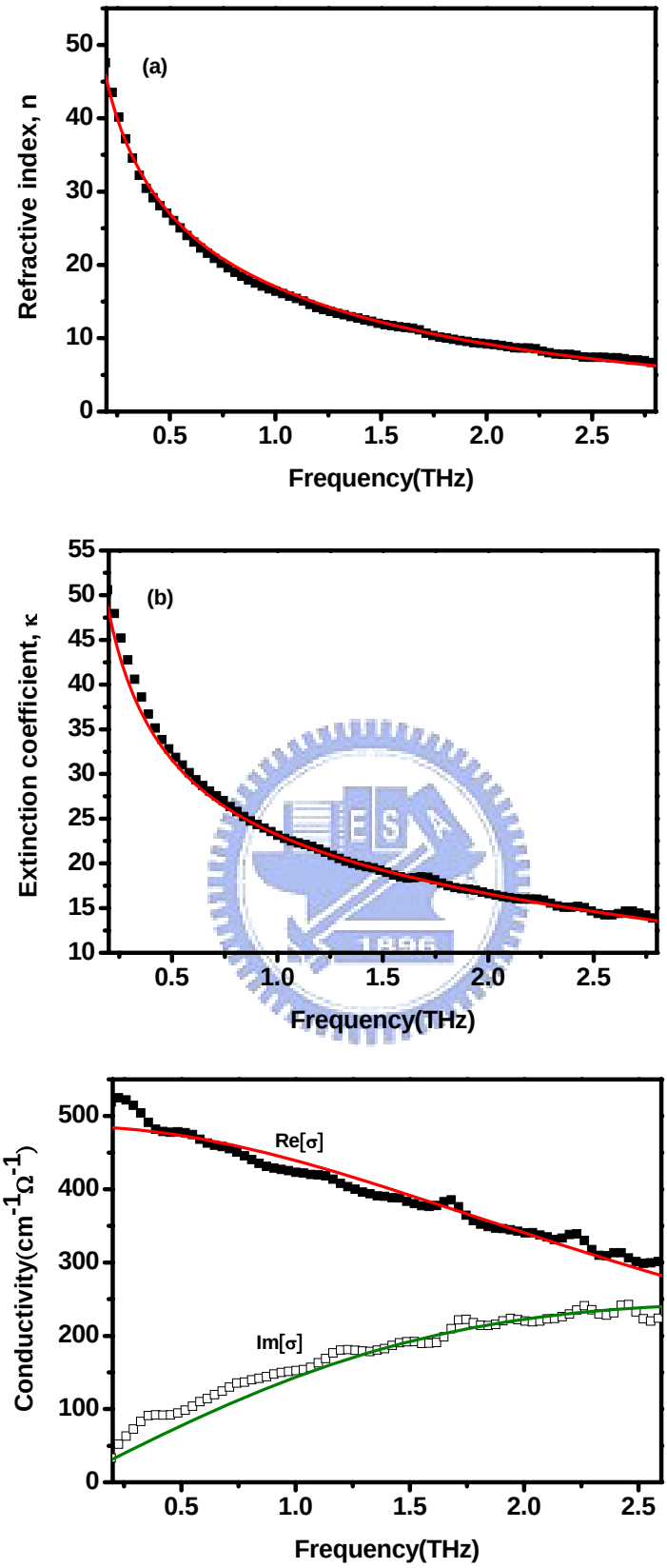

Fig.5-11 Experimental data (square) and fitting curves (solid line) of (a) Refractive index, (b) Extinction coefficient and (c) complex conductivity of InN (A)

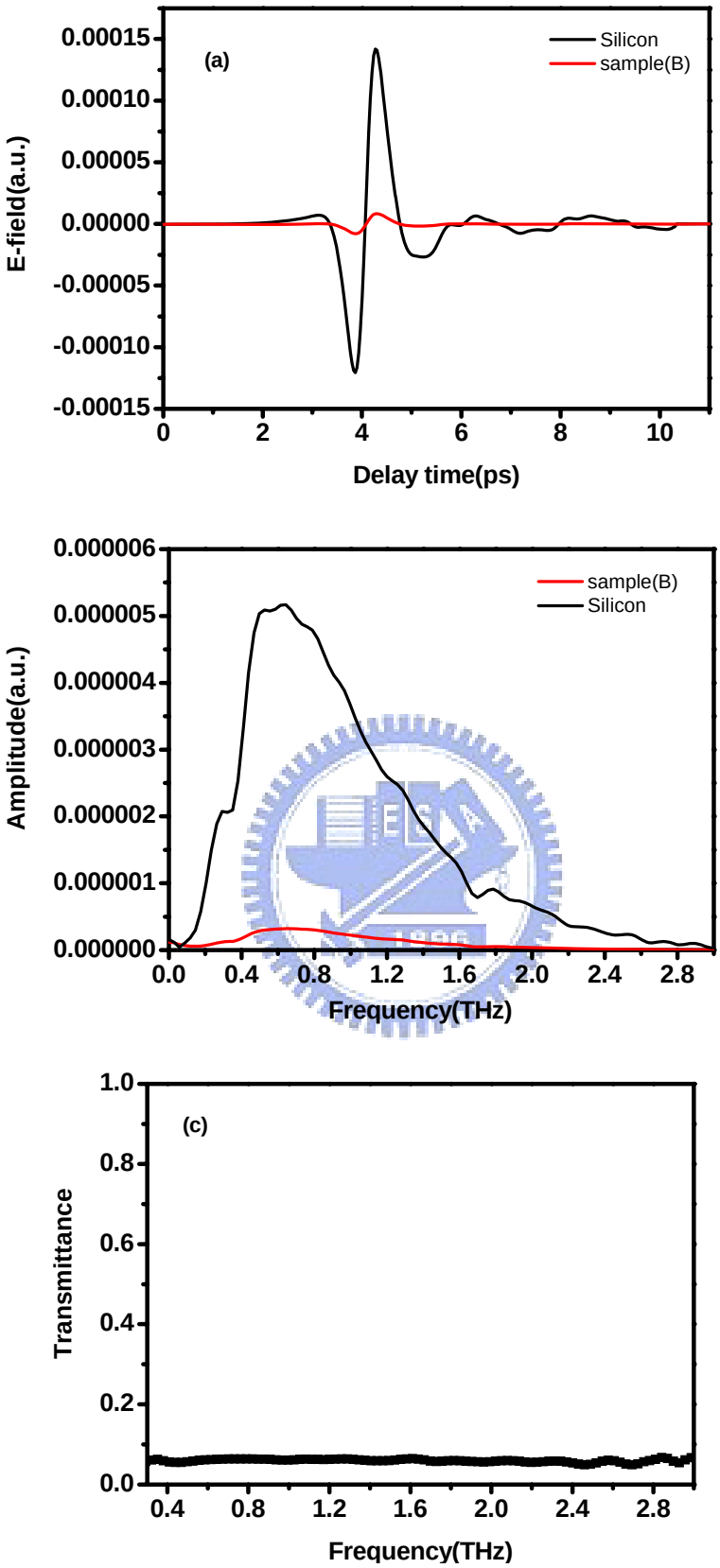

Fig.5-12 (a) THz time-domain waveforms transmitted through InN sample (A) and silicon substrate, and (b) their corresponding Amplitude spectrums. (c) The amplitude transmittance of the InN sample (B).

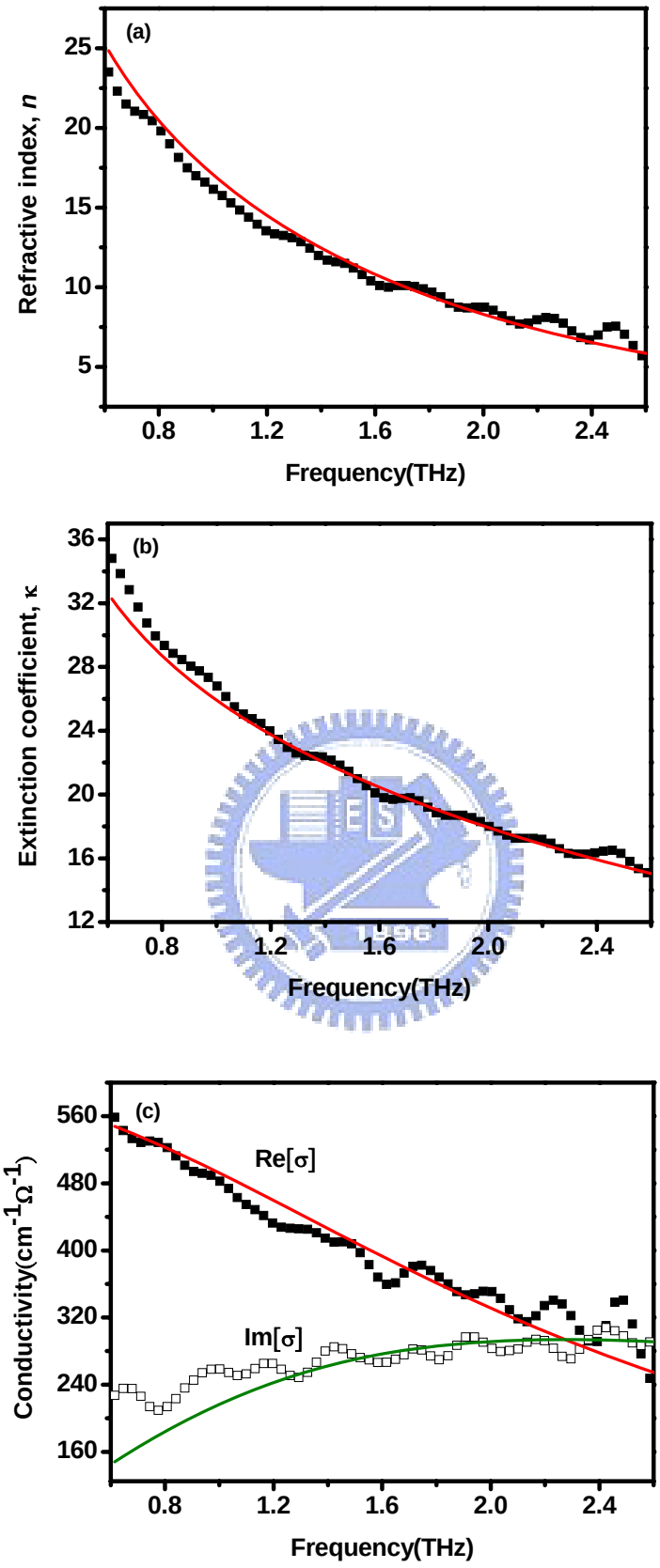

Fig.5-13 Experimental data (square) and fitting curves (solid line) of (a) Refractive index, (b) Extinction coefficient and (c) complex conductivity of InN (B)

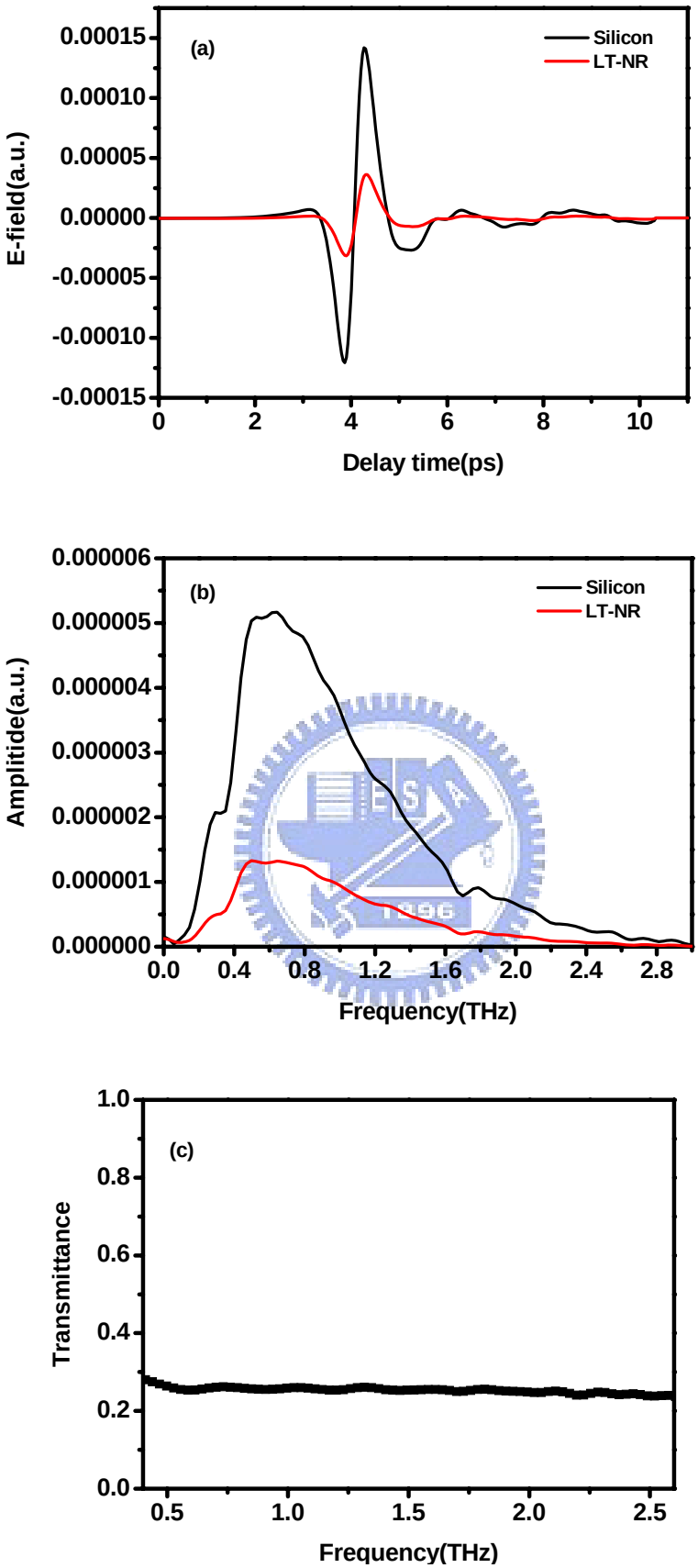

Fig.5-14 (a) THz time-domain waveforms transmitted through LT-NR and silicon substrate, and (b) their corresponding Amplitude spectrums. (c) The amplitude transmittance of LT-NR.

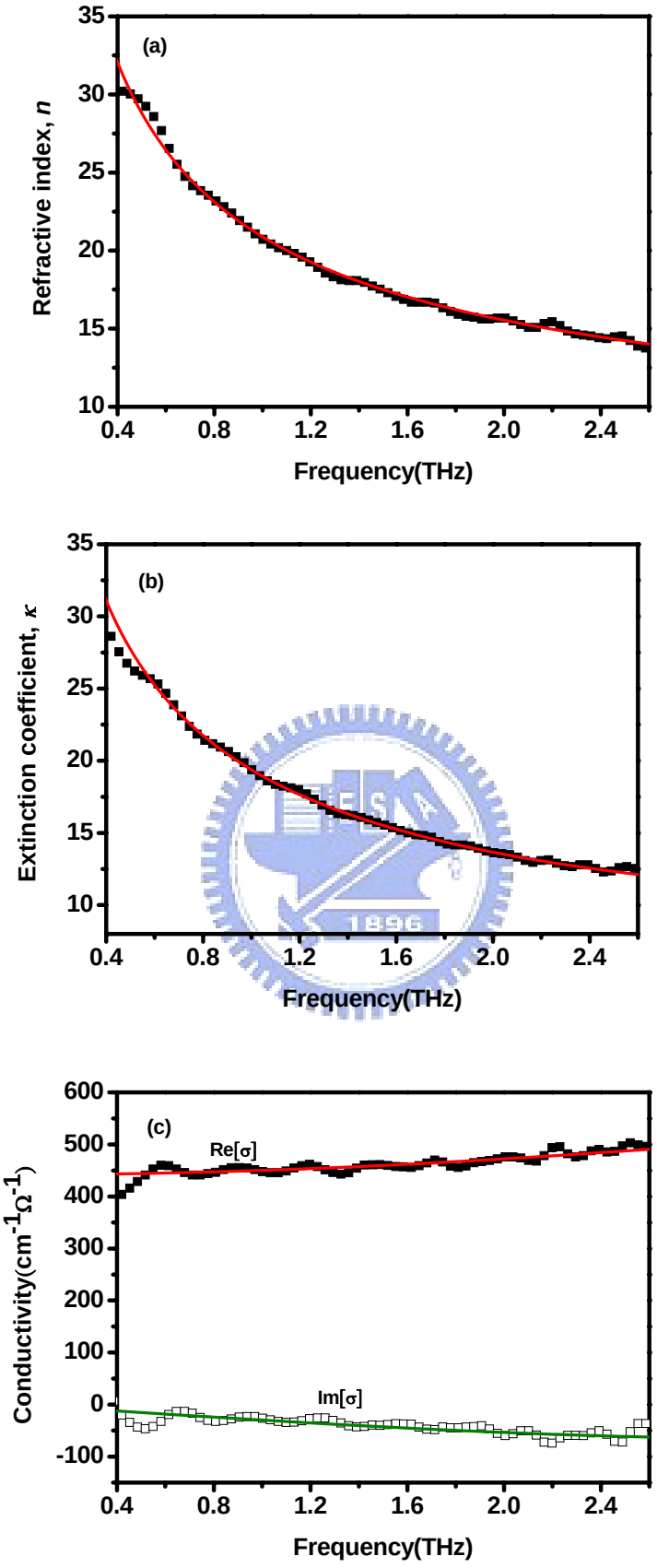

Fig.5-15 Experimental data (square) and fitting curves (solid line) of (a) Refractive index, (b) Extinction coefficient and (c) complex conductivity of LT-NR

5.2 Transient Carrier Dynamics of InN

For this work, the samples were measured by optical pump-terahertz probe system as described in 4.2.3. We use 800nm (1.55ev) light to generate photo-electrons in InN-epilayer and LT-NR with energy bandgap about 0.7ev to investigate the transient carrier dynamics. The photo-electrons with excess energy of 0.85ev which is far below the distance between the conduction minimum to the next local minimum are confined within Γ valley without intervalley scattering. We monitor the peak amplitude of THz waveform, T, as a function of delay time between the terahertz and 800nm optical pump pulse. The differential transmission $\Delta T / T_0$ of both samples are plotted in Fig. 5-17 at 1900 $\mu J / cm^2$ pump fluence where T_0 is the THz peak amplitude before optical excitation. The peak amplitudes decrease 70% and 25% after excitation for InN-epilayer and LT-NR, respectively, and then gradually recover due to the recombination and trapping events that decrease the number of mobile electron and reduce the photoconductivity. The optical pump pulse absorbed and scattered by the InN-epilayer and LT-NR are about 80% and 95%, respectively, but the change of peak amplitude of LT-NR is much less than that of InN-epilayer. Terahertz absorption by the photo-electrons is because of acceleration of the free carriers generated by optical pump pulse, but the free carriers generated in LT-NR are confined within the nanostructure and have much lower mobility (62cm^2/Vs) than that of InN-epilayer that make the terahertz absorption by LT-NR much less than by InN epilayer. The decay curves shown in Fig.5-16 are fit with a sum of two exponential terms [11]:

$$\frac{\Delta T}{T_0} = \Delta T_{\max}(A_1 e^{\frac{-t}{\tau_1}} + A_2 e^{\frac{-t}{\tau_2}}) \qquad (5\text{-}1)$$

Where A_1 A_2 (A_1+A_2=1) are weighting factors and τ_1, τ_2 are decay time constants. The fitting results are listed in Table 5-1.The fast decay time of LT-NR is about 2.6ps

which is much faster than that of epilayer (30.7ps). We propose that the fast decay time is mainly controlled by trapping events, and trapping of mobile electrons in nanorods occurs mainly at surface and interface and is strongly affected by surface area due to the surface or trap states increase with increasing surface area. For the nanorods morphology, electrons interact more frequently with surface resulting in a fraction of them are captured by surface and the rest of them are scattered. The trapping time (2.6ps) is longer than carrier scattering time (13fs) obtained from fit of Drude-Smith model and therefore electrons can interact with surface many times before being trapped. The much longer decay time of LT-NR is because of free carriers excited in the silicon substrate in which carriers have nanosecond to millisecond life time. The optical pump-terahertz probe results are consistent with previous results of static optical constants characterization that the nanorods morphology causes electrons to be confined within nanostructure and interact with surface by scattering or trapping.

	A_1	A_2	τ_1(ps)	τ_2(ps)
Epilayer	0.71	0.29	193.5	30.7
LT-NR	0.88	0.12	7839	2.6

Table.5-1 Bi-exponential decay fit of time-solved data shown in Fig.5-19

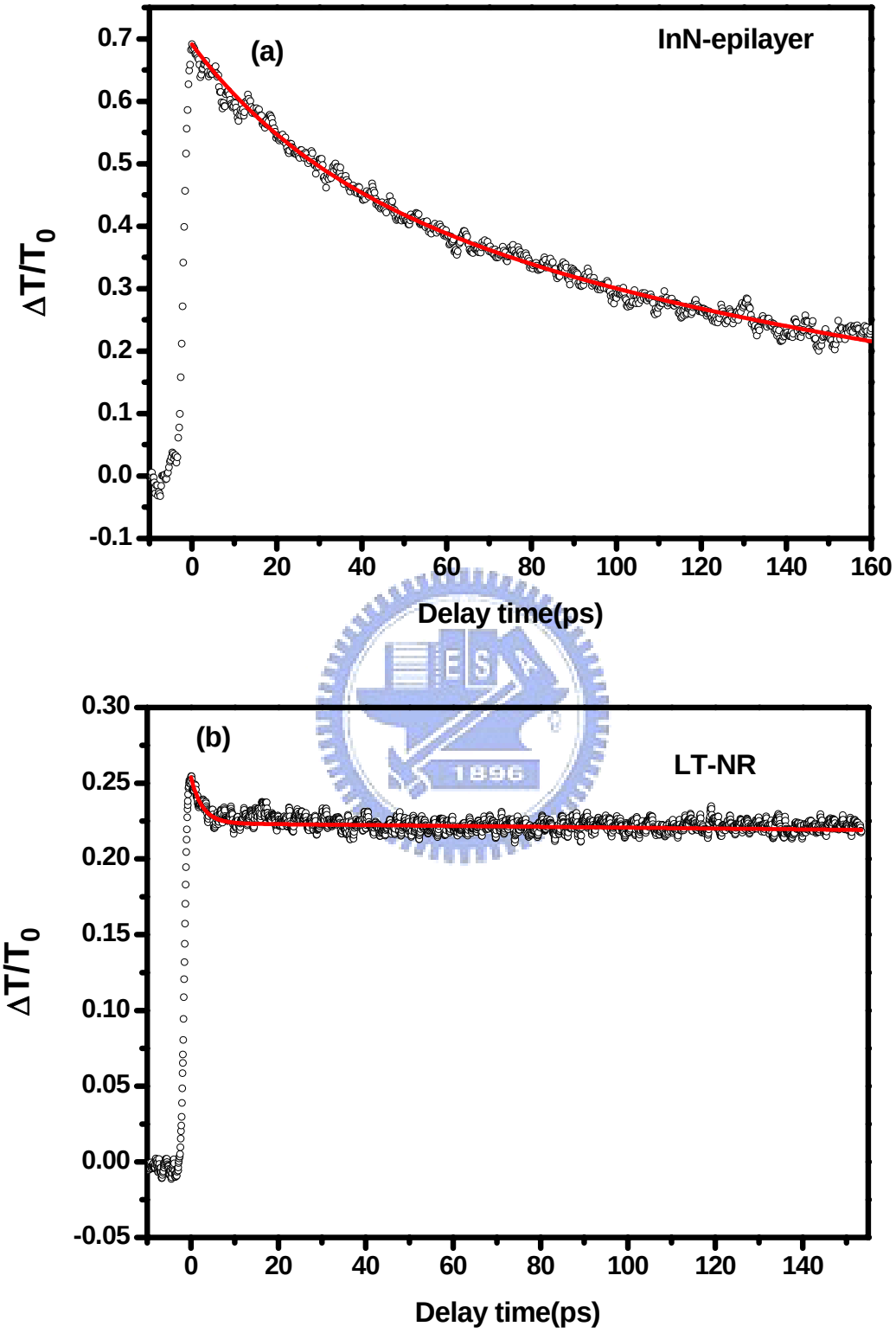

Fig.5-16 Relative differential transmission as a function of pump-probe delay time (open circle) for (a) InN-epilayer and (b) LT-NR comparison with a bi-exponential decay model (solid line)

5.3 Terahertz Emission from InN Surface

For this work, three InN emitters were measured by electro-optic THz system. The photo-exciting beam is collimated on the samples with a spot size of ~ 2 mm at the angle of incidence of 70˚, which is near the Brewster angle. The emitted THz pulses were detected by free-space electro-optic sampling in a 2-mm-thick ZnTe crystal as a function of delay time with respect to the optical pump pulse. We have also investigated the azimuthal angle dependence of THz emission, which reflects the contribution of optical rectification effect. No significant dependence was observed for all three samples.

Fig. 5-17~5-19 shows the time-domain waveforms and their corresponding amplitude spectrums of THz emission for LT-NR, HT-NR, and the InN epilayer, respectively. Each sample is excited at the laser fluence of 720 μ J/cm^2. The bandwidth of each emitter is up to 2.5THz. The dependence of peak amplitude of THz emission on the pump power is plotted in Fig. 5-20. The peak THz amplitudes of HT-NR and InN film increase by about twice as the pump power increases by as much as ten times, while that of LT-NR increases at least six times. Excited by laser pulses at 1 mJ/cm^2, the THz emission from LT-NR is about three times stronger than that from InN thin film and HT-NR.

THz radiation from the narrow bandgap semiconductor is generated by the ultrafast-laser-driven accelerated carriers formed in a shallow surface area. Therefore, efficient THz emission from these materials is closely related to the near-surface characteristics of the materials, including their morphology, point defects, and the effective surface area. For InN film, since the surface accumulation layer is typically very thin (~ 10 nm) compared to the penetration depth of the laser pulse [29], its contribution to the total THz radiation is negligible compared to the photo-Dember

effect [16] [14]. Moreover, for *n*-type InN with a high carrier concentration, the direction of surface field is opposite to the photo-Dember field and consequently reduces the total magnitude of THz radiation. Room-temperature polarized Raman spectroscopic studies [27] showed that the concentrations of free carriers in nanorods are one order of magnitude higher than that in the InN film, suggesting that there are a considerable amount of structural defects in the LT-NR. Further, Room-temperature photoluminescence (PL) signals of HT-NR and LT-NR are about one to two orders of magnitude lower than that of the InN film [27]. This phenomenon has been attributed to strong surface electron accumulation effect, which screens photocarriers and in turn reduces the radiative recombination in InN nanorods.

Nanorods have drastically increased effective surface area compared to the film and every surface exposed to the photo-excitation pulses may participate in absorption. In order to investigate the relation between the surface area and optical absorption, we studied the reflectance of each sample. Measured nearly-normal-incident reflectance in Fig. 5-21 demonstrates that over the whole range of excitation level, absorption in nanorods (~ 95 %) is much larger than that in the film (~ 80 %). And it may correspond to the enhanced optical absorption in nanorods by increased effective surface area. Here one must notice that HT-NR absorbs as much of excitation energy as LT-NR, while THz radiation from HT-NR in Fig. 5-20 is much lower than that from LT-NR. This inefficient conversion of optical absorption to THz emission in HT-NR may be understood by the nanorod-size dependence of THz emission. Since the penetration depth of the laser pulse in the nanorod is limited by its geometrical shape, the surface-to-volume ratio becomes the crucial factor for the optical absorption and THz emission.

The radius of large-size nanorods formed in both LT- and HT-NR is about 65 nm.

This is smaller than the penetration depth of the laser pulse, but still larger than the surface accumulation layer. Since the surface field is opposite in direction to the photo-Dember field, if we exclude the accumulation layer (~ 10 nm) from the total volume of nanorods, THz radiation by the photo-Dember field is mainly generated in the inner volume with the radius of ~ 55 nm. Meanwhile, the ultra-small nanorods in HT-NR have much smaller radius (~ 30 nm) and their effective volume of THz radiation is as small as the inner volume with the radius of 20 nm. Under the assumption that THz emission from surface accumulation layer is negligible because of screening, we can roughly calculate the effective volume of THz emission by the nanorods solely due to the photo-Dember effect. Comparing with LT-NR, the number of large-size nanorods of HT-NR reduces by ~ 40 % (see FE-SEM images in Fig. 3-2). On the other hand, there is about three times more number of ultra-small nanorods with small effective volume closely packing the space between large-size nanorods. Although there are much more nanorods including both large-size and ultra-small rods, the total effective volume of THz emission for HT-NR is about twice smaller than that for LT-NR. As the excitation power increases, the absorption and THz emission in LT-NR increase accordingly due to its large effective volume. In contrast, the increased absorption in the ultra-small nanorods of HT-NR may not be effectively converted into the THz emission due to the decreased effective volume.

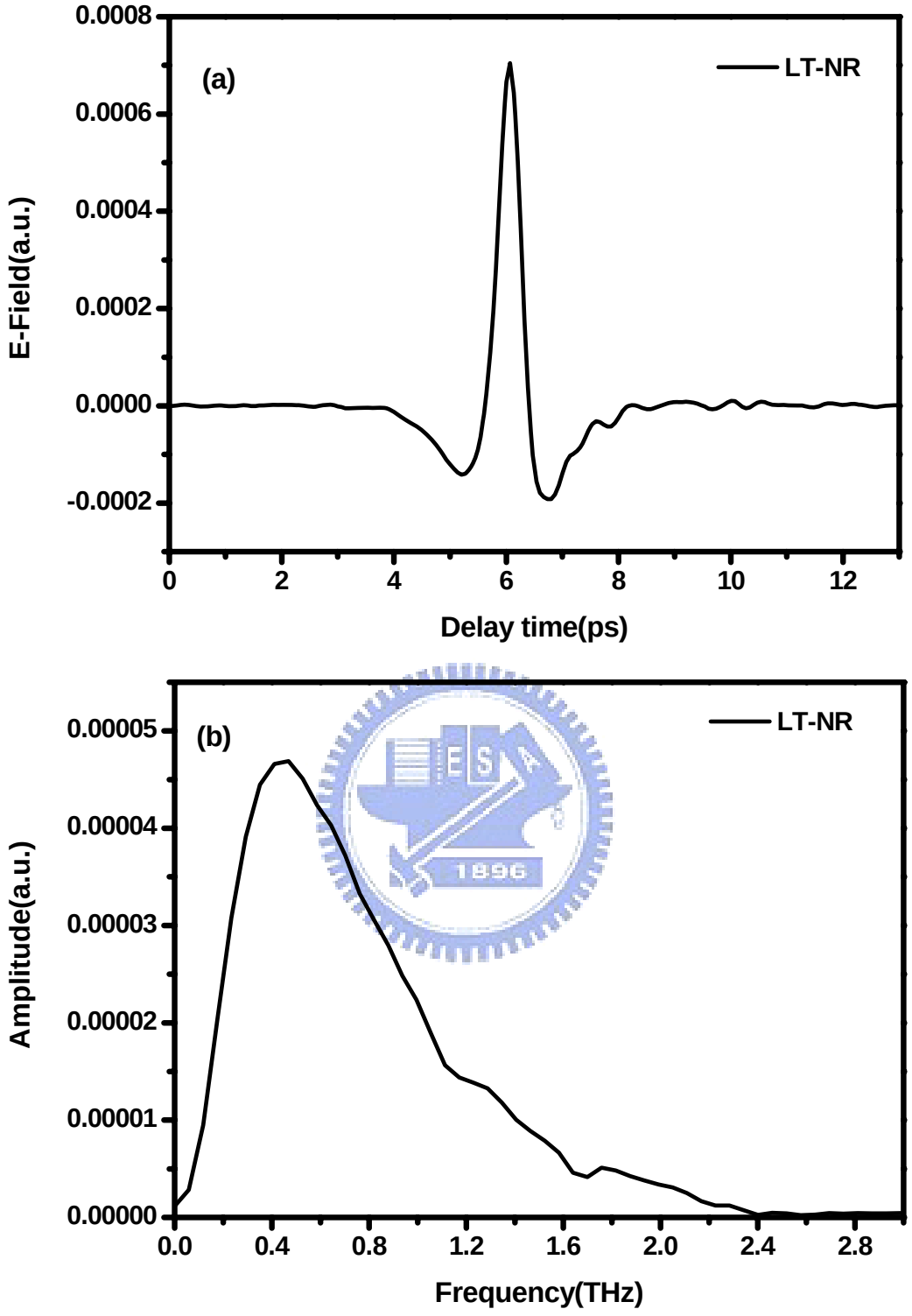

Fig.5-17 THz (a) time-domain waveform and (b) corresponding amplitude spectrum generated from LT-NR

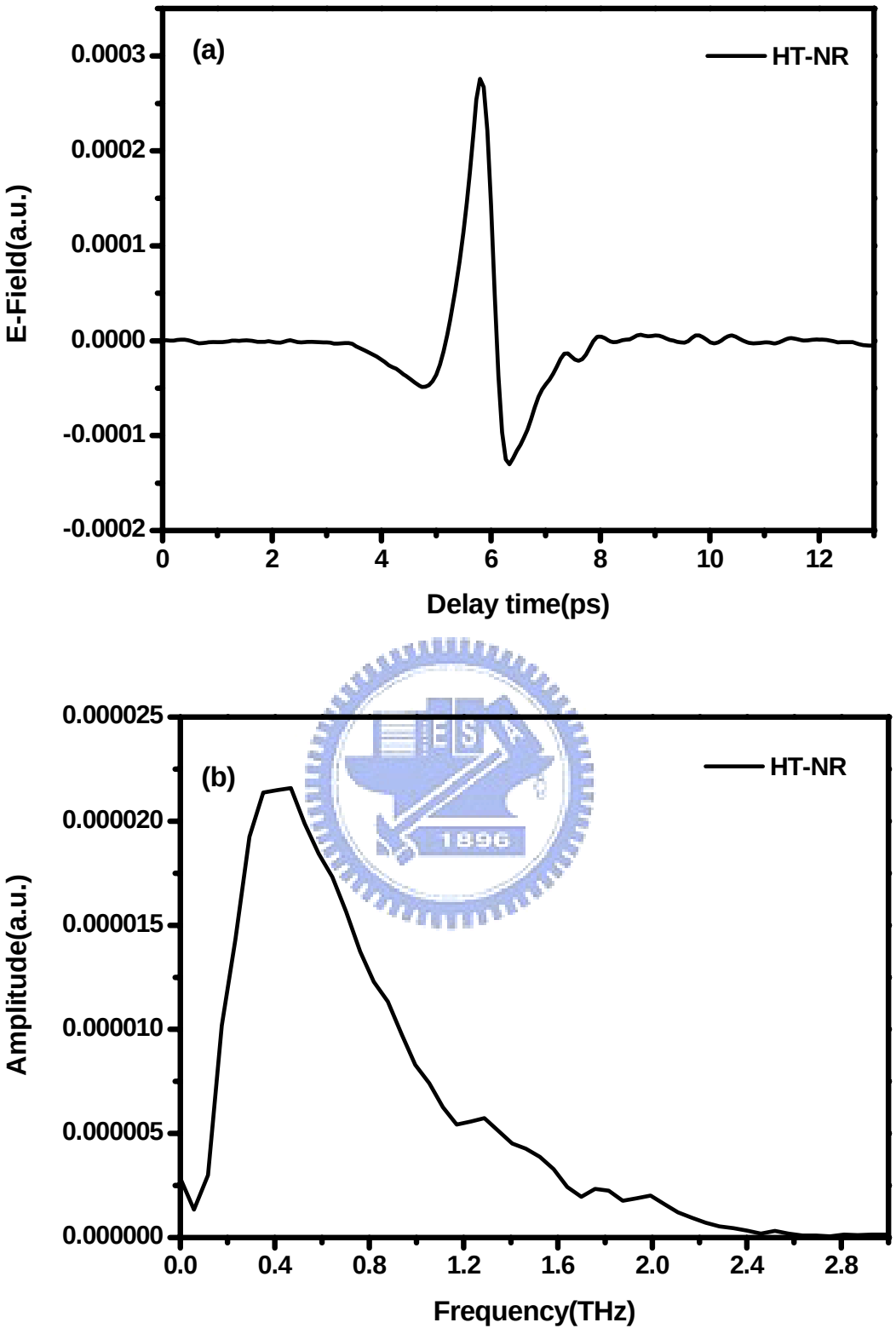

Fig.5-18 THz (a) time-domain waveform and (b) corresponding amplitude spectrum generated from HT-NR

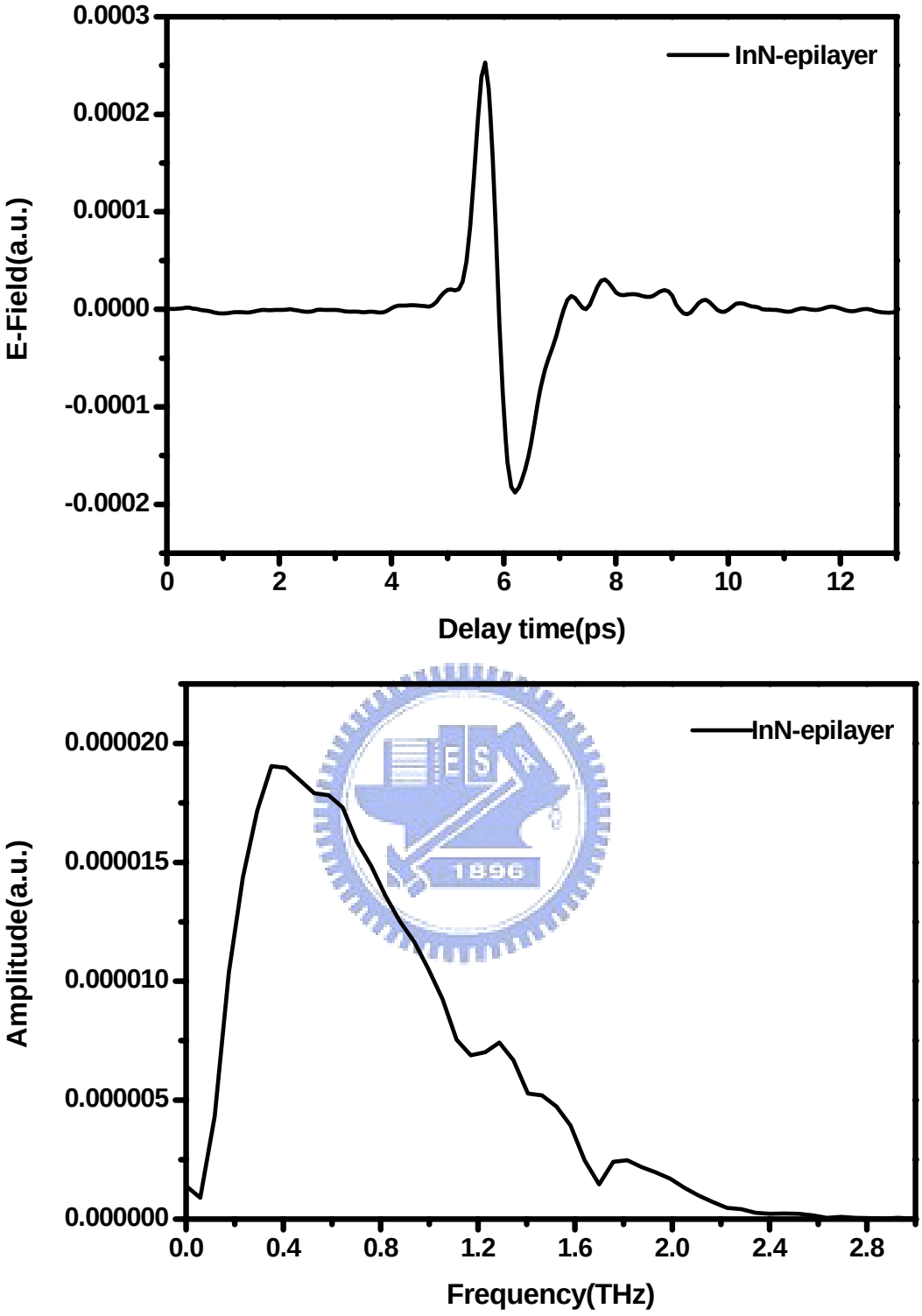

Fig.5-19 THz (a) time-domain waveform and (b) corresponding amplitude spectrum generated from InN-epilayer

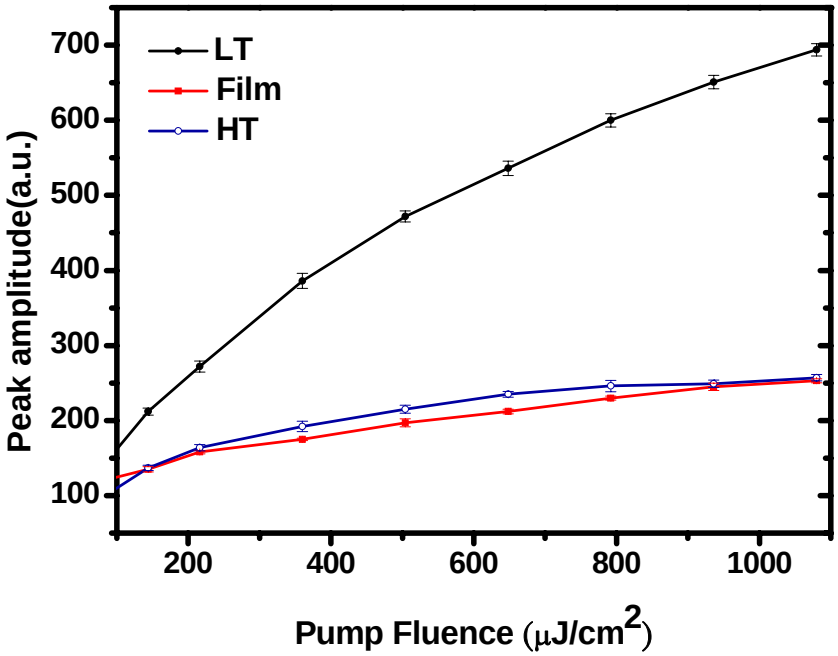

Fig.5-20 Peak amplitude of THz emission for InN film (solid squares), HT- (open circles) and LT-NR (solid circles) as a function of laser pump power

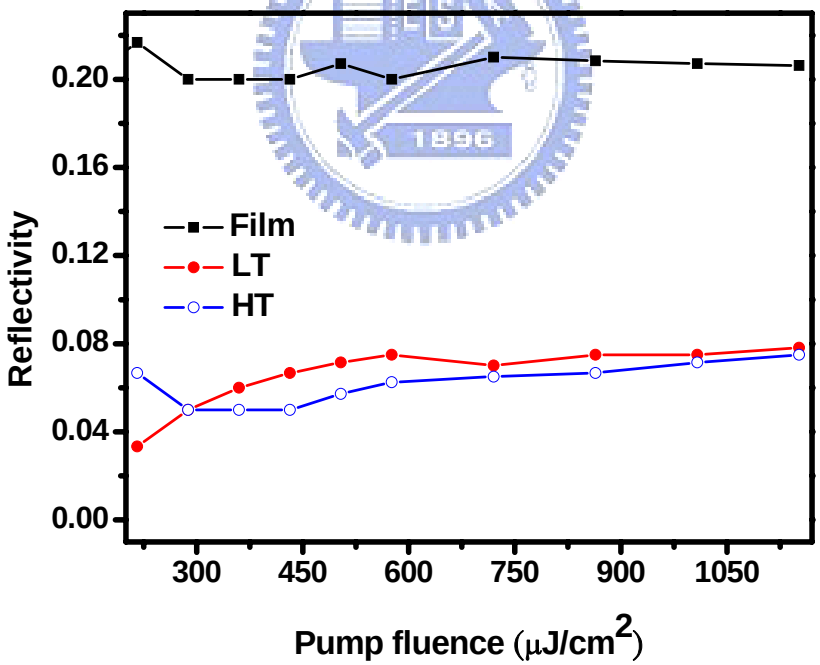

Fig. 5-21 Optical reflectivities in HT-NR (open circles), LT-NR (solid circles), and InN-epilayer (solid squares) as a function of excitation energy. Optical absorption in InN film is about 80 %, while that in nanorods is about 95 %.

6. Conclusions and Future Work

6.1 Conclusions

In this thesis, we have investigated physical parameters of the InN and GaN films and their nanorods in THz range. The simple-Drude model was used to describe the epitaxial films, while the Drude-Smith model for InN nanorods. The mobility and the carrier density of GaN and InN films obtained from the THz time-domain spectroscopy are consistent with those from the Hall effect measurement. Non-Drude-like behavior of GaN and InN nanorods might be attributed to localization or backscattering of carriers within the nanorods. In optical pump-terahertz probe study, we have investigated the transient carrier dynamics of InN-epilayer and its nanorods. The reduced photoconductivity of InN nanorods in comparison with epilayer has been attributed to the small mobility due to localization of electrons, and the faster recovering time of photoconductivity is because of the increased defect and trap states due to the nanorods morphology.

For THz emission study, we demonstrated that the enhancement of THz emission from InN nanorods. The “screened” photo-Dember effect is found to be the main THz emission mechanism in InN nanorods. The enhancement of THz emission is closely related to the surface-to-volume ratio of the nanorods. Nanorods with the radius smaller or comparable to the thickness of the accumulation layer do not contribute significantly to THz emission.

6.2 Future Work

Nanostructured materials, such as GaN nanorods and ZnO nanowires, have the abundant potentials in the optoelectronic applications. The study of these wide bandgap semiconductors are limited by the lack of an intense light source with the photon energy larger than their bandgaps. Currently, we are working on the

sum-frequency generation of 400nm and 800nm for better understanding of these materials.

Reference

[1] Auston D H, Cheung K P and Smith P R, "Picosecond photoconducting Hertzian dipoles," *Appl. Phys. Lett.,* vol.45, pp. 284–6, 1984

[2] Rice,A. *et al.* "Terahertz optical rectification from <110> zinc-blende crystals," *Appl. Phys. Lett.,* vol.64, pp. 1324–1326, 1994.

[3] X.-C. Zhang, B. B. Hu, J. T. Darrow, and D. H. Auston, "Generation of femtosecond electromagnetic pulses from semiconductor surfaces," *Appl. Phys. Lett*., vol.56, pp. 1011-1013, 1990.

[4] R. Kohler, et al., "Terahertz semiconductor heterostructure laser," *Nature,* vol. 417, pp. 156-159, 2002.

[5] Q. Wu, and X.-C. Zhang, "Free-space electro-optic sampling of terahertz beams," *Appl. Phys. Lett.,* vol. **6,** pp. 3523–3525, 1995.

[6] A. G. Markelz, A. Roitberg, and E. J. Heilweil, "Pulsed terahertz spectroscopy of DNA, bovine serum albumin and collagen between 0.1 and 2.0 THz," *Chem. Phys. Lett.* vol. **320,** pp. 42–48, 2000.

[7] B.B. Hu and M. C. Nuss, "Imaging with terahertz waves," *Opt. Lett.,* vol. 20, pp. 1716–1718, 1995

[8] D. Grischkowsky, S. Keiding, M. van Exter, and Ch. Fattiger, "Far-infrared Time-domain Spectroscopy with Terahertz Beams of Dielectrics and Semiconductors," *J. Opt. Soc. Am. B*, vol. 7, No. 10, pp. 2006-2015, 1990.

[9] M. van Exter and D. Grischkowsky, "Optical and Electronic Properties of Doped Silicon From 0.1 to 2 THz," *Appl. Phys. Lett*., vol. 56, no. 17, pp. 1694-1696 1990.

[10] Matthew C. Beard, Gordon M. Turner, James E. Murphy, Olga I. Micic, Mark C. Hanna, Arthur J. Nozik, and Charles A. Schmuttenmaer, " Electronic Coupling in InP Nanoparticle Arrays" *Nano Lett*., vol. 3 pp. 1695-1699

[11] Jason B. Baxter and Charles A. Schmuttenmaer, “Conductivity of ZnO Nanowires, Nanoparticles, and Thin Films Using Time-Resolved Terahertz Spectroscopy,” *J. Phys. Chem. B*, vol. 110, pp.25229-25239, 2006

[12] D. G. Cooke, A. N. MacDonald,1 A. Hryciw, J. Wang,Q. Li, A. Meldrum, and F. A. Hegmann, “Transient terahertz conductivity in photoexcited silicon nanocrystal films,” *Phys. Rev. B,* vol.73, pp. 193311-1-193311-4, 2006

[13] V.Yu. Davydov, A.A. Klochikhin, R.P. Seisyan, V.V. Emtsev, S.V. Ivanov, F. Bechstedt, J. Furthmüller, H. Harima, A.V. Mudryi, J. Aderhold, O. Semchinova, and J. Graul, “Absorption and Emission of Hexagonal InN. Evidence of Narrow Fundamental Band Gap,” *Phys. Status Solidi B,* vol. 229, pp. r1-r3, 2002

[14] R. Acsazubi, I. Wilke, K. Denniston, H. L. Lu, and W. J. Schaff, “Terahertz emission by InN,“ *Appl. Phys. Lett.,* vol.**84**, pp. 4810-4812, 2004.

[15] G. D. Chern, E. D. Readinger, H. Shen, M. Wraback, C. S. Gallinat, G. Koblmuller, and J. S. Speck, “Excitation wavelength dependence of terahertz emission from InN and InAs,” *Appl. Phys. Lett.*, vol.**89**, pp.141115, 2006.

[16] B. Pradarutti, G. Matthaus, C. Bruckner, S. Riehemann, G. Notni, S. Nolti, V. Cimalla, V. Lebedev, O. Ambacher, and A. Tunnermann, “ InN as THz Emitter excited at 1060 nm and 800 nm,” *Proc. of SPIE,* vol. 6194, pp.619401, 2006.

[17] P.K. Benicewicz, J.P. Roberts, and A.J. Taylor, “Scaling of terahertz radiation from large-aperture boased photoconductors,” *J. OPT. Soc. Am. B,* vol. 11, pp. 2533-2545, 1994.

[18] X.-C. Zhang and D.H.Auston, “Optoelectronic measurement of semiconductor surface and interface with femtosecond optics,” *J. Appl. Phys*., vol.71 pp.326-338, 1991

[19] W. Monch, “Semiconductor Surface and Interface,” Springer, Berlin, Heidelberg pp. 68, 1993

[20] D. Mittleman, “Sensing with Terahertz Radiation,” Springer, Berlin, Heidelberg pp.155, 2002

[21] David K. Cheng, „Field and wave Electromagnetics 2/e“, 2nd Ed., Addison-Wesley, 1989.

[22] N. W. Ashcroft and N. D. Mermin, “*Solid State Physics,”* Saunders College Publishing, Philadelphia, 1976

[23] N. V. Smith, “Classical generalization of the Drude formula for the optical conductivity,” *Phys. Rev. B,* vol.64, pp.155106, 2001

[24] S. Gwo, C.-L. Wu, C.-H. Shen, W.-H. Chang, T. M. Hsu, J.-S. Wang, and J.-T. Hsu, “Heteroepitaxial growth of wurtzite InN films on Si(111) exhibiting strong near-infrared photoluminescence at room temperature,” *Appl. Phys. Lett.,* vol. 84, pp. 3765-3767, 2004.

[25] C.-H. Shen, H.-Y. Chen, H.-W. Lin, S. Gwo, A. A. Klochikhin, and V. Yu. Davydov, “Near-infrared photoluminescence from vertical InN nanorod arrays grown on silicon: Effects of surface electron accumulation layer,” *Appl. Phys. Lett.,* vol. 88, pp. 253104, 2006.

[26] A. S. Barker, Jr. and M. Ilegems, “Infrared Lattice Vibrations and Free-Electron Dispersion in GaN,” *Phys. Rev. B,* vol. **7**, pp. 743-750, 1973.

[27] H.-Y. Chen, C.-H. Shen, H.-W. Lin, C.-H. Chen, C.-Y. Wu, S. Gwo, A. A. Klochikhin, and V. Yu. Davydov, “Near-infrared photoluminescence of vertically aligned InN nanorods grown on Si(111) by plasma-assisted molecular-beam epitaxy,” *Thin Solid Films*, vol. 515, pp.961-966, 2006.

[28] T. Hofmann, T. Chavdarov, V. Darakchieva, H. Lu,W. J. Schaff, and M. Schubert, “ Anisotropy of the Γ-point effective mass and mobility in hexagonal InN,” *Phys. Status Solidi c,* vol. 3, pp. 1854-1857, 2006.

[29] I. Mahboob, T. D. Veal, L. F. J. Piper, and C. F. McConville, Hai. Lu and W. J. Schaff, J. Furthmüller, and F. Bechstedt, “Intrinsic Electron Accumulation at

Clean InN Surfaces," *Phys. Rev. Lett*., vol. 92, pp. 036804, 2004.

[30] F. J. Garcı´a-Vidal, J. M. Pitarke, and J. B. Pendry, "Effective Medium Theory of the Optical Properties of Aligned Carbon Nanotubes," *Phys. Rev. Lett*., vol.78, pp. 4289-4292, 1997